

Attoseconds and the exascale: on laser plasma surface interactions



Robin Timmis
Your College
University of Oxford

A thesis submitted for the degree of
Doctor of Philosophy

Michaelmas 2014

Acknowledgements

Personal

Institutional

The author thanks the Norreys Research Group, Prof. Philip Burrows and Dr. Qingsong Feng for useful discussions, the SMILEI consortium and the ARCHER2 support team. The authors also acknowledge the support of AWE plc, UKRI-EPSRC and the Oxford-Berman Graduate Scholarship program. This work used the ARCHER2 UK National Supercomputing Service (<https://www.archer2.ac.uk>) under project e674 of UKRI-EPSRC grant no. EP/R029148/1 and UKRI-STFC grant no. ST/V001655/1.

Abstract

The commissioning of multi-petawatt class laser facilities around the world is gathering pace. One of the primary motivations for these investments is the acceleration of high-quality, low-emittance electron bunches. Here we explore the interaction of a high-intensity femtosecond laser pulse with a mass-limited dense target to produce MeV attosecond electron bunches in transmission and confirm with three-dimensional simulation that such bunches have low emittance and nano-Coulomb charge. We then perform a large parameter scan from non-relativistic laser intensities to the laser-QED regime and from the critical plasma density to beyond solid density to demonstrate that the electron bunch energies and the laser pulse energy absorption into the plasma can be quantitatively described via the Zero Vector Potential mechanism. These results have wide-ranging implications for future particle accelerator science and associated technologies.

Contents

List of Figures	ix
A List of Symbols and Abbreviations	xi
1 Introduction	1
1.1 High-energy-density physics	1
1.2 Electromagnetism fundamentals	5
1.3 The definition of a plasma	6
1.3.1 The Debye length	7
1.3.2 The plasma parameter	8
1.3.3 Collisionality and the plasma frequency	9
1.4 The Lawson-Woodward theorem	10
1.5 Laser-solid density plasma linear interaction	11
1.6 Relativity	12
1.6.1 Ultra-relativistic similarity theory	14
1.6.2 Relativistic lasers and plasmas	16
1.6.3 Conservation of generalised transverse momentum	16
1.7 QED effects	17
1.7.1 High-energy photon emission and radiation reaction	18
1.7.2 Multi-photon Breit-Wheeler pair production	19
1.8 Simulating the interaction	19
1.8.1 Supercomputing resources	20
1.8.2 Particle-In-Cell codes	20
2 Attosecond X-ray harmonics on the ORION laser facility	29
2.1 A plan	29
2.2 Theory	30
2.2.1 The ROM model	30
2.2.2 The normalisation factor	30
2.2.3 Hole boring	31
2.3 Experimental data processing	36
2.3.1 Image plate calibration	36
2.3.2 OHREX calibration	38
2.3.3 Extracting the data	39

Appendices

References

47

List of Figures

1.1	Laser systems across the globe, both commissioned and theorised. . .	4
1.2	Diagram to illustrate the derivation of the plasma frequency.	10
1.3	A schematic of the PIC code loop and the algorithms performed. . .	21
1.4	A representation of the staggered Yee grid.	22
1.5	Smilei simulation box decomposition into cells, patches and MPI patch collections.	25
1.6	Representation of the interaction of the ARCHER2 hardware and software components when running Smilei.	26
2.1	2D PIC simulation of HHG beaming effect via hole boring.	32
2.2	Unprocessed IP from ORION experiment	40
2.3	Typical ORION experiment uncalibrated IP response quartz ($10\bar{1}0$) crystal and Fourier transform	41
2.4	Typical ORION experiment calibrated IP response for the quartz ($10\bar{1}1$) crystal.	43

A List of Symbols and Abbreviations

Note	All quantities are defined in SI units unless otherwise specified throughout the thesis.
α	Twiss parameter = $-\frac{\langle x_i x'_i \rangle}{\epsilon_{\text{rms}}^i}$
a_0	Normalised vector potential = $\frac{e \mathbf{E}_L }{m_e c \omega_L}$
A	Atomic mass number
\mathbf{A}	Three-vector potential
\mathbf{A}^μ	Four-vector potential = $(\phi/c, \mathbf{A})$
β	Normalised speed = v/c or Twiss parameter = $\frac{\langle x_i \rangle}{\epsilon_{\text{rms}}^i}$
β	Normalised velocity = \mathbf{v}/c
\mathbf{B}	Magnetic field
\mathbf{B}_L	Magnetic field of a laser pulse
c	Speed of light = $3.00 \times 10^8 \text{ m s}^{-1}$
δ	Skin depth
$\delta(\mathbf{x})$	Dirac-delta function
$d\mathbf{s}$	Vector line element
Δ	Change in a variable
D	Number of dimensions
∇	Partial derivative = $\hat{\mathbf{x}}_\mu \frac{\partial}{\partial x_\mu}$, $\mu = x, y, z$
ϵ_0	Permittivity of free space = $8.854 \times 10^{-12} \text{ F m}^{-1}$
ϵ_{rms}	Transverse geometric emittance
$\epsilon_{\text{n,rms}}$	Transverse normalised emittance
e	Absolute charge of an electron = $1.602 \times 10^{-19} \text{ C}$
e^\pm	Electron (−) or positron (+)
\mathbf{E}	Electric field
E_S	Schwinger electric field = $1.3 \times 10^{18} \text{ V m}^{-1}$

\mathbf{E}_L	Electric field of a laser pulse
f	Distribution function
\mathbf{F}_L	Lorentz force = $q(\mathbf{E} + \mathbf{v} \times \mathbf{B})$
γ	Lorentz/gamma factor = $\frac{1}{\sqrt{1-\beta^2}}$ or Twiss parameter = $\frac{\langle x_i'^2 \rangle}{\epsilon_{\text{rms}}^i}$ or high-energy photon
η	Efficiency
I	Electromagnetic field intensity
\mathcal{H}	Hamiltonian
θ	Angle of incidence of a laser pulse
\mathbf{J}	Current density
\mathbf{k}	Electromagnetic three-wave vector
\mathbf{K}^μ	Electromagnetic four-wave vector = $(\omega/c\mathbf{k})$
K	Boltzmann constant = $1.38 \times 10^{-23} \text{ J K}^{-1}$
λ_D	Debye length $\equiv \sqrt{\frac{\epsilon_0 K T_e}{n_e e^2}}$
λ_L	Laser pulse wavelength
Λ_ν^μ	Lorentz transformation matrix
L	Length
\mathcal{L}	Lagrangian
μ_0	Vacuum permeability = $1.257 \times 10^{-6} \text{ N A}^{-2}$
m_e	Mass of an electron = $9.11 \times 10^{-31} \text{ kg}$
n	Harmonic order
n, N	Number
n_c	Plasma critical density = $\frac{\omega_L^2 m_e \epsilon_0}{e^2}$
n_e	Plasma electron number density
\bar{n}_e	Normalised plasma electron number density = $\frac{n_e}{n_c}$
n_i	Plasma ion number density
\mathbf{n}	Vector normal to a surface
N_A	Avogadro's number
N_D	Number of particles within the Debye sphere = $\frac{4}{3}\pi\lambda_D^3 n$
ω	Angular frequency of an oscillation or low energy photon
ω_L	Laser pulse angular frequency

ω_p	Plasma frequency = $\sqrt{\frac{e^2 n_e}{m_e \epsilon_0}}$
ϕ	Angle of laser polarisation out of the plane of interaction or scalar electromagnetic potential
\mathbf{p}	Three-momentum
\mathbf{P}	Pressure
\mathbf{P}^μ	Four-momentum = $(U/c, \mathbf{p})$
Q	Charge
ρ	Density
r_L	Relativistic Larmor radius = $\frac{\gamma m_e v}{e \mathbf{B} }$
\mathbf{r}	Radial vector
$\hat{\mathbf{r}}$	Radial unit vector
R	Rate
σ	Surface area
S	Relativistic similarity parameter = \bar{n}_e/a_0
$S(\mathbf{x})$	Shape function
τ	Average time or standard deviation of time
t	Time
T	Kinetic energy
T_e	Plasma electron temperature
u, v	Speed
\mathbf{u}, \mathbf{v}	Velocity
U	Energy
v_ϕ	Phase velocity
V	Potential or volume
w_L	Beam waist
w_p	Quasi-particle weight
χ_γ	Photon quantum parameter
x, y, z	Standard Cartesian coordinates in 3D
$\mathbf{x}, \mathbf{y}, \mathbf{z}$	Vectors along each axis of the Cartesian coordinate system
$\hat{\mathbf{x}}, \hat{\mathbf{y}}, \hat{\mathbf{z}}$	Unit vectors along each axis of the Cartesian coordinate system
Z	Ion charge state in units of e

Subscripts . . .	The following are defined the subscripts
C	Pseudocapacitor
e	Electron
γ	Photon
L	Laser pulse or Longitudinal
T	Transverse to a laser pulse
pol	Along the polarisation vector of a laser pulse
\perp	Perpendicular
\parallel	Parallel
i, j	Indices
s	Species
x, y, z	Along the specific Cartesian axes
∞	
The hat symbol	To represent a normalised vector
primed coordinates	Field and reference frames
1D, 2D, 3D . . .	One-, two- or three-dimension(al)
BW	Breit-Wheeler
CLF	Central Laser Facility
CPA	Chirped Pulse Amplification
CSE	Coherent Synchrotron Emission
FDTD	Finite Difference Time Domain
HB	Hole Boring
HED	High-Energy-Density
HHG	High Harmonic Generation
HPC	High Performance Computing
OHREX	ORION High Resolution X-ray
PIC	Particle-In-Cell
QED	Quantum Electro-Dynamics
ROM	Relativistic Oscillating Mirror
RPM	Relativistic Plasma Mirror
RR	Radiation Reaction
SF-QED	Strong-Field Quantum Electro-Dynamics
ZVP	Zero Vector Potential

1

Introduction

Contents

1.1	High-energy-density physics	1
1.2	Electromagnetism fundamentals	5
1.3	The definition of a plasma	6
1.3.1	The Debye length	7
1.3.2	The plasma parameter	8
1.3.3	Collisionality and the plasma frequency	9
1.4	The Lawson-Woodward theorem	10
1.5	Laser-solid density plasma linear interaction	11
1.6	Relativity	12
1.6.1	Ultra-relativistic similarity theory	14
1.6.2	Relativistic lasers and plasmas	16
1.6.3	Conservation of generalised transverse momentum	16
1.7	QED effects	17
1.7.1	High-energy photon emission and radiation reaction	18
1.7.2	Multi-photon Breit-Wheeler pair production	19
1.8	Simulating the interaction	19
1.8.1	Supercomputing resources	20
1.8.2	Particle-In-Cell codes	20

1.1 High-energy-density physics

We sit on the verge of the exa-scale revolution both in terms of computing [kotheExascaleComputingUnited2019] and laser power. With rapid adoption

of the pioneering advancements of Chirped Pulse Amplification (CPA) by Strickland and Mourou [stricklandCompressionAmplifiedChirped1985] and of Optical Parametric Chirped Pulse Amplification [rossOpticalParametricChirped2000], multi-petawatt facilities have now been commissioned and built across the globe and plans for sub-exawatt facilities are underway. Figure 1.1 details the parameter space accessible by current and proposed facilities [stricklandCompressionAmplifiedChirped1985, fourmauxPedestalCleaningHigh2011, wang085PWLaser2017, tiscarenoOhioStateUniversity42PW202017, rossGenerationTerawattPulses2000, yangMultiterawattLaserSystem2006, witte2006source, stoecklHighEnergyPetawattProject2006, lozhkarevCompact56Petawatt2006, herrmannGenerationSubthreecycle162009, andriukaitis90GWPeak2011, zhaoGeneration120GW2013, hoppsOverviewLaserSystems2013, hoppsOverviewLaserSystem2013, thire10MJ5cycle2015, yinHighefficiencyOpticalParametric2016, galesExtremeLightInfrastr2016, OMEGAFacility, renCompactDoublepassRaman2008, lanciaExperimentalEvidenceShort2008, lanciaSignaturesSelfSimilarRegime2016, marquesJouleLevelHighEfficiencyEnergy2019, thebergeTunableUltrashortLaser2006, trushinSub10fsSupercontinuumRadiation2007, ohIntenseTerahertzGeneration2013, horioGenerationSub17Fs2014, takahashiGeneration100fs2014, goulieimakisSingleCycleNonlinearOptics2008, skantzakisCoherentContinuumExtreme2009, ferrariHighenergyIsolatedAttosecond2010, takahashiAttosecondNonlinearOptics2013, popmintchevUltravioletSurpriseEfficient2015, nomuraAttosecondPhaseLocking2009, bierbachGeneration10Relativistic2012, heisslerMultimJHarmonicEmission2015, yeungExperimentalObservationAttosecond2017, jahnIntenseIsolatedAttosecond2019, rusEfficientHighbrightnessSoftxray1997, sebbanFullCharacterizationHighgain2000, rusMultimillijouleHighlyCoherent2002, zeitounHighintensityHighlyCoherent2004, wangHighBrightnessInjectionSeededSoftXRayLaser2006, rohringerAtomicInnershellXray2006, ayvazyanFirstOperationFreeelectron2006, ackermannOperationFreeelectronLaser2007, emmaFirstLasingOperation2010, FlashFreeElectronLaser, FlashFreeElectronLaser, FELIXLaboratoryOverview, FELIXLaboratoryOverview, FELIXLaboratoryOverview, kneipObservationSynchrotronRadiation2008, kneipBrightSpatiallyCoherent2010, juEnhancementXraysGenerated2012, chenBrightBetatronXray2013, wangQuasimonoenergylaser2013, coleLaserwakefieldAcceleratorsHard2015, wenzQuantitativeXrayPhasecontrast2015,

taphuocAllopticalComptonGammaray2012, chenMeVEnergyRaysInverse2013,
tsaiCompactTunableCompton2015, polyanskiyPicosecondPulseAmplification2011,
haberbergerFifteenTerawattPicosecond2010, glowniaAmplification193nmFemtosecon
kandoEnhancementPhotonNumber2009, obenschainHighenergyKryptonFluoride2015
trinesSimulationsEfficientRaman2011, trinesSimulationsEfficientRaman2011,
kawanakaConceptualDesignSubexawatt2016, tajimaMarriage20keVSuperconducting2

clearly, there is no indication of wavering interest or support for the field of High-Energy-Density (HED) physics.

HED physics is the laboratory study of the behaviour of matter with a pressure above 10 GPa, approximately one million atmospheres and containing free electrons not confined to a solid state [**drakeFocusHighEnergy2014**], typically in the plasma state of matter. HED conditions are found for a vast range of densities and temperatures (from zero to a million million Kelvin) operating in both the quantum and relativistic realms. The applications are equally diverse, including but not limited to inertial confinement fusion, particle acceleration for scientific or medical purposes and light sources for diagnostic tools. Ubiquitous in the natural universe, beyond our solar system, all that can be observed in the sky is radiation emitted from HED plasmas [**chen**].

This thesis concerns itself with a specific interaction, that of a high-power short-pulse laser incident on a flat solid target. Through the process discussed in this thesis, using state-of-the-art 10 PW laser facilities such as [**galesExtremeLightInfrastructure2018**], electron bunches and light pulse of unprecedented charge and brightness can be produced, both with attosecond duration, thus uncovering new avenues for attosecond resolution diagnostics and to access the Schwinger limit. Seemingly counter-intuitively, as the laser power increases, via relativistic effects and for certain conditions, greater coherency in the electron dynamics can be observed and the signals amplified. The red dashed line of figure 1.1 could be accessed using next generation sub-etawatt facilities. Before delving into this fascinating phenomenon, the remainder of this chapter will provide some of the relevant background information. Chapter ?? introduces the Zero Vector Potential of

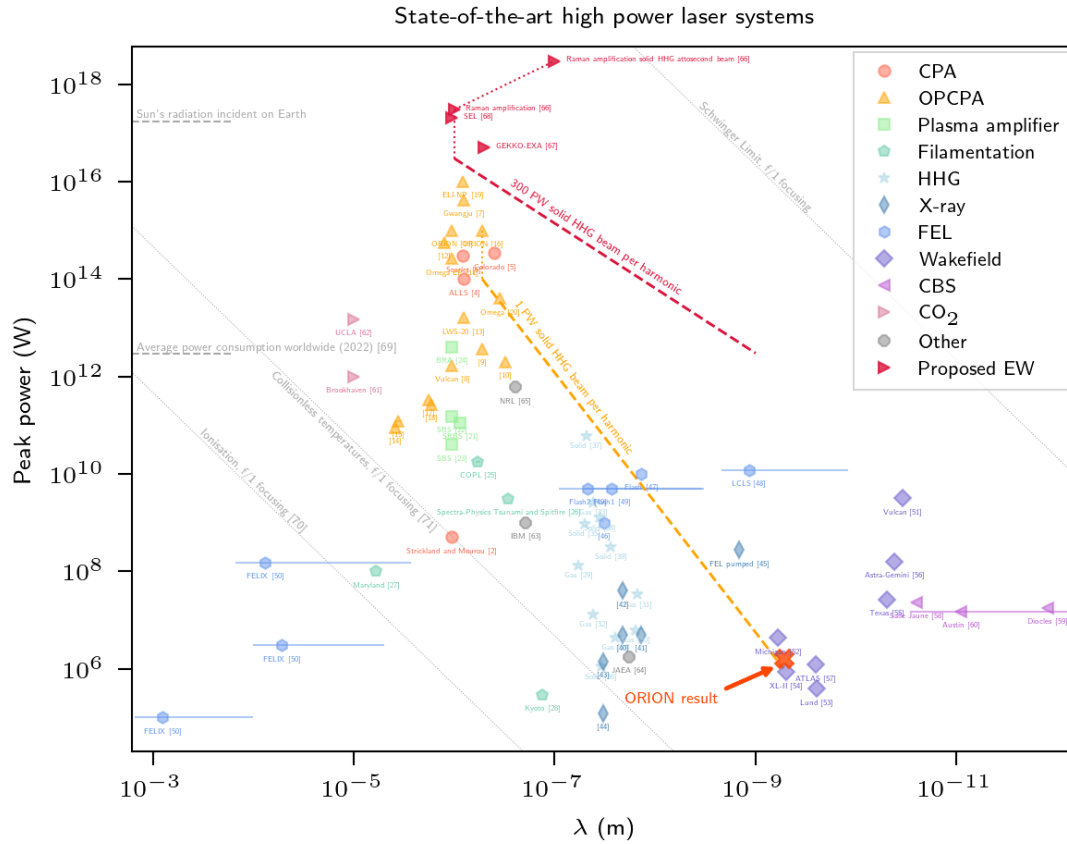


Figure 1.1: A by no means exhaustive plot of laser systems across the globe, both commissioned and theorised [stricklandCompressionAmplifiedChirped1985, fourmauxPedestalCleaningHigh111, wang085PWLaser2017, tiscarenoOhioStateUniversity2020, sung42PW202017, rossGenerationTerawattPulses2000, yangMultiterawattLaserSystem2002, witte2006source, stoecklHighEnergyPetawattProject2006, lozhkarevCompact56Petawatt2007, herrmannGenerationSubthreecycle162009, andriukaitis90GWPeak2011, zhaoGeneration120GW2013, hoppsOverviewLaserSystems2013, hoppsOverviewLaserSystems2013, thire10MJ5cycle2015, yinHighefficiencyOpticalParametric2016, galesExtremeLightInfrastructure2018, OMEGAFacility, renCompactDoublepassRaman2008, lanciaExperimentalEvidenceShort2010, lanciaSignaturesSelfSimilarRegime2016, marquesJouleLevelHighEfficiencyEnergy2019, thebergeTunableUltrashortLaser2006, trushinSub10fsSupercontinuumRadiation2007, ohIntenseTerahertzGeneration2013, horioGenerationSub17Fs2014, takahashiGeneration10uJCoherent2002, goulieimakisSingleCycleNonlinearOptics2008, skantzakisCoherentContinuumExtreme2009, ferrariHighenergyIsolatedAttosecond2010, takahashiAttosecondNonlinearOptics2013, popmintchevUltravioletSurpriseEfficient2015, nomuraAttosecondPhaseLocking2009, bierbachGeneration10Relativistic2012, heisslerMultimJHarmonicEmission2015, yeungExperimentalObservationAttosecond2017, jahnIntenseIsolatedAttosecond2019, rusEfficientHighbrightnessSoftxray1997, sebbanFullCharacterizationHighgain2000, rusMultimillijouleHighlyCoherent2002, zeitounHighintensityHighlyCoherent2004, wangHighBrightnessInjectionSeededSoftXRayLaser2017, rohringerAtomicInnershellXray2012, ayvazyanFirstOperationFreeelectron2006, ackermannOperationFreeelectronLaser2007, emmaFirstLasingOperation2010, FlashFreeElectronLaser, PRAFT Printed on March 12, 2024, FlashFreeElectronLaser, FELIXLaboratoryOverview, FELIXLaboratoryOverview, FELIXLaboratoryOverview, kneipObservationSynchrotronRadiation2008, kneipBrightSpatiallyCoherent2010, juEnhancementXraysGenerated2012,

attosecond absorption in this laser-solid interaction. The following chapter discusses the associated process of Surface High Harmonic Generation and the results of a recent experiment at the ORION laser facility where the absolute intensity of individual X-ray harmonics was measured and compared to the theory.

1.2 Electromagnetism fundamentals

The spatio-temporal propagation of electric $\mathbf{E}(t, \mathbf{x})$ and magnetic $\mathbf{B}(t, \mathbf{x})$ fields must satisfy Maxwell's equations [**chenIntroductionPlasmaPhysics2016**]

$$\nabla \cdot \mathbf{B} = 0, \quad (1.1a)$$

$$\nabla \cdot \mathbf{E} = \frac{\rho}{\epsilon_0}, \quad (1.1b)$$

$$\nabla \times \mathbf{B} = \mu_0 \mathbf{J} + \mu_0 \epsilon_0 \partial_t \mathbf{E}, \quad (1.1c)$$

$$\nabla \times \mathbf{E} = -\partial_t \mathbf{B}. \quad (1.1d)$$

Here, $\epsilon_0 = 8.85 \times 10^{-12} \text{ F m}^{-1}$ and $\mu_0 = 1.26 \times 10^{-6} \text{ N A}^{-2}$ are the vacuum permittivity and permeability respectively and $\rho(t, \mathbf{x})$ and $\mathbf{J}(t, \mathbf{x})$ the total charge and current densities of charged particles present.

A particle with charge q and velocity \mathbf{v} in the presence of electromagnetic fields experiences the Lorentz force,

$$\mathbf{F}_L = q(\mathbf{E} + \mathbf{v} \times \mathbf{B}). \quad (1.2)$$

The electromagnetic fields can be obtained from the scalar, ϕ , and vector, \mathbf{A} , potentials as [**steaneRelativityMadeRelatively2012**]

$$\mathbf{E} = -\nabla \phi - \partial_t \mathbf{A}, \quad (1.3)$$

$$\mathbf{B} = \nabla \times \mathbf{A}. \quad (1.4)$$

The Vlasov-Maxwell system of equations

A collisionless and fully ionised plasma is fully described in the kinetic description by the Vlasov-Maxwell system of equations [derouillatSmileiCollaborativeOpensource2018]. Each plasma species, s , of particles with mass m_s and charge q_s is described by its distribution function $f_s(t, \mathbf{x}, \mathbf{p})$ at time t , position \mathbf{x} and momentum $\mathbf{p} = m_s \gamma \mathbf{v}$. The distribution satisfies the Vlasov equation, that is,

$$(\partial_t + \frac{\mathbf{p}}{m_s \gamma} \cdot \nabla + \mathbf{F}_L \cdot \nabla_{\mathbf{p}}) f_s = 0, \quad (1.5)$$

where \mathbf{F}_L is the Lorentz force given in equation 1.2. The electric $\mathbf{E}(t, \mathbf{x})$ and magnetic $\mathbf{B}(t, \mathbf{x})$ fields that generate the force must satisfy Maxwell's equations (equations 1.1).

This self-consistent system of equations describes the dynamics of plasma particles within electromagnetic fields. The particles modify the fields via their charge and current densities,

$$\rho(t, \mathbf{x}) = \sum_s q_s \int d^3p f_s(t, \mathbf{x}, \mathbf{p}), \quad (1.6)$$

and

$$\mathbf{J}(t, \mathbf{x}) = \sum_s q_s \int d^3p \mathbf{v} f_s(t, \mathbf{x}, \mathbf{p}), \quad (1.7)$$

respectively.

1.3 The definition of a plasma

As outlined in F. Chen's definitive textbook 'Introduction to Plasma Physics and Controlled Fusion' [chenIntroductionPlasmaPhysics2016], a plasma must fulfil three criteria, namely,

1. Ionisation: a plasma must consist of both charged and neutral particles, of course this alone cannot define a plasma, any gas will contain some degree of ionisation, however, with reference to figure 1.1, clearly, modern high power laser systems will instantaneously fully ionise a target upon incidence;

2. Quasineutrality: while locally there can be (often extreme) electromagnetic forces and charge concentrations at work, over the length scales of the plasma, such forces are screened out and the plasma bulk remains net neutral in charge;
3. Collective behaviour: unlike in a gas, where collisions will dominate the dynamics, the particles in a plasma generate electromagnetic fields that interact at a distance and thus a particle's motion depends not only on its immediate vicinity but on the surrounding plasma conditions, indeed often it is the so-called *collisionless* plasmas where collisions can be safely neglected that are of most interest, as is the focus of this thesis.

These conditions can be quantitatively described by the Debye length, the plasma parameter and the plasma frequency as laid out in the following sections.

1.3.1 The Debye length

The Debye length describes the extent to which a plasma can shield electromagnetic fields within and so remain quasineutral. Consider an infinitely extending plasma with a test charge placed at some point, then what would be the scalar potential $\phi(\mathbf{x})$ around it? If the plasma had no kinetic energy, the charged particles would arrange themselves immediately adjacent to the test charge and once this equilibrium state was reached there would be no electromagnetic fields present. More realistically, the plasma will have some temperature, likely a very large temperature and so some particles will be able to escape the potential of the test charge and thus leak electromagnetic fields into the plasma bulk. Poisson's equation (equation 1.1b in the static case) reads

$$\epsilon_0 \nabla^2 \phi = -e(Zn_i - n_e), \quad (1.8)$$

where $\epsilon_0 = 8.854 \times 10^{-12} \text{ F m}^{-1}$ is the permittivity of free space, $e = 1.602 \times 10^{-19} \text{ C}$ is the charge of an electron, Z is the plasma ion charge in units of e and n_i and n_e are the number densities of plasma ions and electrons.

Since the electrons are significantly more mobile than the ions due to their lower mass, it is in general the electrons and not the ions that respond to the test charge and the ions can be assumed to provide a constant background of positive charge density. If the number density of electrons follows a Boltzmann temperature distribution in the presence of a potential energy $-e\phi$, then

$$n_e = n_{e,0} e^{e\phi/KT_e}, \quad (1.9)$$

where $n_{e,0}$ is the electron number density far from the test charge, $n_i = n_{e,0}/Z$, $K = 1.38 \times 10^{-23} \text{ J K}^{-1}$ is the Boltzmann constant and T_e is the electron temperature in Kelvin. Note that in plasmas it is very common for different species to have differing temperatures depending on the mechanism for energy absorption and the timescales for collisions compared to the timescale of the study.

Substituting equation 1.9 into equation 1.8 and Taylor expanding the exponential term in the limit that the plasma is weakly coupled ($e\phi \ll KT_e$),

$$\nabla^2 \phi = \frac{\phi}{\lambda_D^2}, \quad (1.10)$$

where

$$\lambda_D \equiv \sqrt{\frac{\epsilon_0 K T_e}{n_e e^2}}, \quad (1.11)$$

is the *Debye length* and describes the thickness of the charge sheath surrounding the test charge. For quasineutrality to hold for the plasma bulk, its spatial dimensions, L , must extend beyond a few Debye lengths, *i.e.*

$$L \gg \lambda_D. \quad (1.12)$$

1.3.2 The plasma parameter

In order for the derivation of section 1.3.1 to be statistically valid, there must be a large number of charged particles within the shielding sheath. The number of particles within the *Debye sphere* is

$$N_D = \frac{4}{3} \pi \lambda_D^3 n, \quad (1.13)$$

where, N_D is the *plasma parameter*. Note that, as discussed above, in most cases it is most suitable to choose the number density n to be the number density of electrons, n_e . To ensure the plasma is suitably ionised (criterion 1) and that the plasma engages in collective behaviour (criterion 3),

$$N_D \gg 1. \quad (1.14)$$

1.3.3 Collisionality and the plasma frequency

Collective behaviour not only depends on the ability for large numbers of particles to interact via electromagnetic forces but also that these forces dominate over collisions in describing particle trajectories. Taking ω as the typical frequency of plasma oscillations and τ as the average time between collisions, for a plasma (as opposed to a gas)

$$\omega\tau > 1 \quad (1.15)$$

is required. It now remains to determine what is the typical frequency of collisions in a given plasma. While the types of plasma waves and their associated frequencies of oscillation are multitudinous, the characteristic frequency, the *plasma frequency*, ω_p , is the most straightforward. It describes the response of electrons to charge imbalances within an infinite uniform plasma at rest in the absence of magnetic fields or temperature fluctuations. As noted in section 1.3.1, the ions provide a constant background of positive charge.

Consider an semi-infinite plasma existing for $x > 0$, with electron density n_e and ion density n_e/Z of charge state Z^1 . Suppose the electron fluid is displaced by some perfectly isotropic force into the plasma bulk a distance $(\Delta x)\hat{\mathbf{x}}$ as in figure 1.2. The total charge of displaced electrons within a surface area of σ is

$$Q = -en_e\sigma\Delta x. \quad (1.16)$$

¹This description has direct relevance to the Zero Vector Potential mechanism which will be made clear in chapter ??.

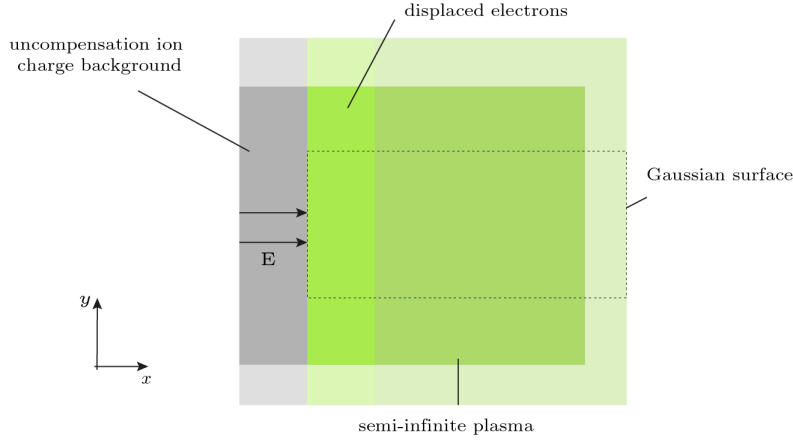


Figure 1.2: The electrons of a semi-infinite plasma are displaced inwards by some external force leaving in their wake an uncompensated space charge of ‘immobile’ positive ions. By constructing a Gaussian surface along the dashed line, using Gauss’ Law, the electric field associated with the positive space charge can be calculated.

Applying the integral from of Gauss’ law (from equation 1.1b) to the surface detailed in figure 1.2, the uncompensated charge leads to

$$-\sigma E \hat{\mathbf{x}} = \frac{Q}{\epsilon_0} \hat{\mathbf{x}} = -\frac{en_e \sigma \Delta x}{\epsilon_0} \hat{\mathbf{x}} \quad (1.17)$$

at the electron surface. By the Lorentz force, equation 1.2, the displaced electrons will experience a restoring force, $-eE\hat{\mathbf{x}}$, perpendicular to the surface due to the electron-ion charge imbalance. The equation of motion for electrons on that surface is therefore

$$m_e \frac{d^2 \Delta x}{dt^2} = -eE = -\frac{e^2 n_e}{\epsilon_0} \Delta x. \quad (1.18)$$

Equation 1.18 clearly describes a simple harmonic oscillator with a characteristic frequency given by the plasma frequency,

$$\omega_p = \sqrt{\frac{e^2 n_e}{m_e \epsilon_0}}. \quad (1.19)$$

1.4 The Lawson-Woodward theorem

The Lawson-Woodward theorem states that there can be no net electron energy gain using laser fields [esareyPhysicsLaserdrivenPlasmabased2009], quite at odds with one of the primary aims of this thesis, that is, the acceleration of electrons. There are, however, several conditions that must be met, namely,

1. The interaction region is infinite;
2. The interaction occurs in a vacuum;
3. The electron is ultra-relativistic ($v \approx c$) along the acceleration gradient;
4. No electro- or magnetostatic fields are present;
5. Non-linear effects are neglected.

Several of these will be applicable to the various accelerations of electrons considered. It is this final condition that is most damning to the application of the theorem. Throughout this thesis the ultra-relativistic laser pulses under consideration ensure non-linear effects cannot be neglected. It is indeed such non-linearities that are of most interest.

1.5 Laser-solid density plasma linear interaction

Consider small transverse electromagnetic waves propagating through a plasma. Linearising equation 1.2 for a single plasma electron by assuming only small field variations and thus small velocity variation,

$$m_e \dot{\mathbf{v}}_e = -e\mathbf{E}. \quad (1.20)$$

Combining the time derivative of equation 1.1c and the curl of equation 1.1d,

$$\nabla \times \nabla \times \mathbf{E} = -\mu_0 \dot{\mathbf{J}} - \mu_0 \epsilon_0 \ddot{\mathbf{E}}. \quad (1.21)$$

Considering only fast oscillations such that ions are effectively immobile,

$$\mathbf{J} = -n_e e \mathbf{v}_e \quad (1.22)$$

and using the identity $\nabla \times \nabla \times \mathbf{E} = \nabla(\nabla \cdot \mathbf{E}) - \nabla^2 \mathbf{E}$,

$$\nabla(\nabla \cdot \mathbf{E}) - \nabla^2 \mathbf{E} = -\frac{\mu_0 n_e e^2}{m_e} \mathbf{E} - \mu_0 \epsilon_0 \ddot{\mathbf{E}}. \quad (1.23)$$

Assuming plane wave solutions of the form

$$\mathbf{E} = \mathbf{E}_0 e^{i(\mathbf{k} \cdot \mathbf{x} - \omega t)}, \quad (1.24)$$

where \mathbf{k} is the wave-vector and ω the frequency of oscillations and noting the waves are transverse $\mathbf{k} \cdot \mathbf{E} = 0$,

$$|\mathbf{k}|^2 \mathbf{E} = -\frac{\mu_0 n_e c^2}{m_e} \mathbf{E} + \mu_0 \epsilon_0 \omega^2 \mathbf{E} \quad (1.25)$$

and hence the dispersion relation for electromagnetic waves propagating in a plasma is

$$\omega^2 = c^2 |\mathbf{k}|^2 + \omega_p^2. \quad (1.26)$$

Equation 1.26 exhibits a *cutoff* dependent on the plasma density via ω_p . The *critical density*, n_c , is defined as the density above which a laser pulse of frequency ω_L cannot propagate through a plasma. This occurs for $\omega_L = \omega_p$, thus,

$$n_c = \frac{m_e \epsilon_0 \omega_L^2}{e^2}. \quad (1.27)$$

As the plane wave has a spatial dependence $\sim \exp(\mathbf{k} \cdot \mathbf{x})$, if $n_e > n_c$, \mathbf{k} is imaginary and the wave no longer propagates through the plasma and instead exponentially attenuates over a skin depth,

$$\delta = \frac{1}{|\mathbf{k}|} = \frac{c}{\sqrt{\omega_p^2 - \omega_L^2}} \quad (1.28)$$

and is reflected. For typical high power lasers with wavelengths in the visible or near-infrared, fully ionised solids tend to have densities well above the critical density and thus

1.6 Relativity

Modern high-power lasers operate in the domain of relativistic mechanics and in general interactions are highly non-linear. It is useful to introduce some of the basic principles of relativity. Note that while there has been growing interest in the curvature of spacetime by relativistic lasers [**atongaGravitationalWavesHighpower2023**], this effect remains undetectable at present. Thus, throughout this thesis the inner product of 4-tensors is defined using the Minkowski Metric [**steaneRelativityMadeRelatively2012**].

Symbol	Name	Components	Invariant
\mathbf{X}^μ	4-displacement	(ct, \mathbf{x})	$-c^2\tau^2$
\mathbf{A}^μ	4-potential	$(\phi/c, \mathbf{A})$	
\mathbf{J}^μ	4-current density	$(c\rho, \mathbf{J})$	$-c^2\rho_0^2$
\mathbf{K}^μ	4-wave vector	$(\omega/c, \mathbf{K})$	
\mathbf{P}^μ	4-momentum	$(U/c, \mathbf{p})$	$-m^2c^2$

Table 1.1: Four-vectors of relevance to this thesis. New parameters are the proper time, τ , the proper charge density, ρ_0 , energy, $U = \gamma mc^2$, three-momentum, $p = \gamma m\mathbf{v}$.

Many useful quantities can be arranged into contravariant four-vectors that undergo a Lorentz transformation for a change of frame of reference [steaneRelativityMadeRelative]. Specifically,

$$\mathbf{A}'^\mu = \Lambda_\mu^\nu \mathbf{A}^\mu, \quad (1.29)$$

where Λ_μ^ν is the appropriate Lorentz transformation, and primed symbols typically denote boosted frames of reference. Without loss of generality, the coordinate system can be defined such that the boosted frame travels along the \mathbf{x} -axis with respect to the initial frame. Thus, the Lorentz transformation is defined

$$\Lambda_\mu^\nu = \begin{pmatrix} \gamma & -\beta\gamma & 0 & 0 \\ -\beta\gamma & \gamma & 0 & 0 \\ 0 & 0 & 1 & 0 \\ 0 & 0 & 0 & 1 \end{pmatrix}. \quad (1.30)$$

Generally, a *beta factor* is a normalised speed or velocity of an object,

$$\beta = \frac{v}{c}, \quad (1.31)$$

here it refers to the frame velocity and its associated Lorentz or *gamma factor* is

$$\gamma = \frac{1}{\sqrt{1 - \beta^2}}. \quad (1.32)$$

Four-vectors relevant this thesis are listed in table 1.1. Transformations of electromagnetic fields under reference frame boosts are given in appendix ?? and Maxwell's equations are Lorentz covariant.

Focusing now on the 4-potential \mathbf{A}^μ , choosing the Lorenz gauge,

$$\partial_\mu \mathbf{A}^\mu = \nabla \cdot \mathbf{A} + \frac{1}{c^2} \partial_t \phi = 0, \quad (1.33)$$

then Maxwell's equations can be written

$$\partial_\nu \partial^\nu \mathbf{A}^\mu = -\frac{1}{c^2 \epsilon_0} \mathbf{J}^\mu. \quad (1.34)$$

Equation 1.34 can then be solved to yield

$$\mathbf{A}(\mathbf{x}, t) = \frac{\mu_0}{4\pi} \int \frac{\mathbf{J}(\mathbf{x}', t_a)}{|\mathbf{x} - \mathbf{x}'|} d^3 \mathbf{x}', \quad (1.35)$$

where $t_a = t - |\mathbf{x} - \mathbf{x}'|/c$ is the advanced time.

1.6.1 Ultra-relativistic similarity theory

Consider a relativistically intense laser pulse normally incident on a collisionless plasma as in figure 1.2 and neglect ion motion. The electron distribution is fully described by the Vlasov equation (equation 1.5) with the self-consistent electric and magnetic fields satisfying Maxwell's equations (equations 1.1). Suppose the incident laser pulse has an initial vector potential

$$\mathbf{A}(t = 0) = \mathbf{a}((y^2 + z^2)/R^2, x/c\tau) \cos k_L x. \quad (1.36)$$

This envelope form for the potential, $\mathbf{a}((y^2 + z^2)/R^2, x/c\tau)$, is sensible provided $k_L R \gg 1$ and $\omega_L \tau \gg 1$, where R is the focal spot radius and τ the pulse duration. For fixed laser envelope, the laser-plasma dynamics depends on just four dimensionless variables: the normalised focal spot size, $k_L R$, the normalised pulse duration, $\omega_L \tau$, the normalised laser vector potential amplitude

$$a_0 = \max \left| \frac{e\mathbf{a}}{m_e c^2} \right|, \quad (1.37)$$

in terms of the peak laser electric field amplitude \mathbf{E}_L ,

$$a_0 = \frac{e|\mathbf{E}_L|}{m_e c \omega_L}, \quad (1.38)$$

and the normalised plasma density

$$\bar{n}_e = \frac{n_e}{n_c}. \quad (1.39)$$

By normalising the system of equations, details given in appendix, and combining these last two expressions into the *relativistic similarity parameter*,

$$S = \frac{\bar{n}_e}{a_0}, \quad (1.40)$$

it is possible to show that in the ultra-relativistic limit ($a_0 \gg 1$), the dynamics of the system is similar for constant S [**gordienkoScalingsUltrarelativisticLaser2005**] with plasma electrons following similar trajectories where

$$\mathbf{p} \sim a_0. \quad (1.41)$$

There is also a more physical meaning to the S parameter. Consider again section 1.5 on the propagation of linear electromagnetic waves through a plasma but now for the case of an ultra-relativistic laser pulse. For an electron rotating in an electromagnetic field,

$$\mathbf{F}_\perp = \gamma m_e \mathbf{a}_\perp, \quad (1.42)$$

where \mathbf{a}_\perp is the acceleration perpendicular to the motion and thus the response of the electrons is reduced by a factor of γ . While some find the *relativistic mass* correction to be somewhat unhelpful nomenclature for the phenomenon [**steaneRelativityMadeRelatively2012**], it has nevertheless become commonplace within the literature of relativistic plasma physics [**umstadterRelativisticLaserPlasma2000**]. Turning the handle, one finds that the relativistic plasma frequency is

$$\omega_p^{\text{rel}} = \sqrt{\frac{e^2 n_e}{\gamma m_e \epsilon_0}}. \quad (1.43)$$

Using equation 1.41, and taking $v \approx c$, then $\gamma \approx a_0$ and the normalised relativistic cutoff density is simply S . Thus, the ultra-relativistic similarity parameter is just a measure of the overdensity of a plasma once relativistic corrections have been applied, *i.e.* for $S > 1$, a laser pulse will be reflection, however for $\bar{n}_e > 1$ and $S < 1$, one enters the regime of relativistically self-induced transparency [**ereminRelativisticSelfInducedTransparency2010**]. It is now possible to define the parameter space of interest in this thesis: relativistic laser plasma surface interactions occur for $a_0 \gg 1$ and $S > 1$.

1.6.2 Relativistic lasers and plasmas

The descriptor *relativistic* is applied liberally in this thesis. When applied to electromagnetic fields or laser pulses it refers to

$$a_0 \geq 1. \quad (1.44)$$

When applied to particles, their Lorentz factors are

$$\gamma = \frac{1}{\sqrt{1 - \beta^2}} \geq 2, \quad (1.45)$$

corresponding to a speed, $u \geq 0.87c$. *Ultra-relativistic* implies these quantities are much larger than the conditions provided. A relativistic laser pulse will accelerate electrons to relativistic velocities in a fraction of a laser pulse cycle. Consider an electron in the presence of a uniform electric field of magnitude $a_0 = 100$, an intensity accessible by current state of the art laser facilities. The work done on that particle by the field is

$$T = (\gamma - 1)m_e c^2 = \int \mathbf{E} \cdot d\mathbf{x}, \quad (1.46)$$

The field will accelerate an electron to relativistic velocities in a distance less than 1 % of a corresponding laser pulse wavelength.

1.6.3 Conservation of generalised transverse momentum

Consider a holonomic system of N relativistic particles under the influence of electromagnetic forces. A particle j with charge e_j and mass m_j experiences a scalar potential,

$$V_j = e_j(\phi - \mathbf{A} \cdot \mathbf{v}_j) \quad (1.47)$$

and hence the system is described by the Lagrangian [goldsteinClassicalMechanics2013]

$$\mathcal{L} = \sum_{j=1}^N \left(-m_j c^2 \sqrt{1 - \beta_j^2} - e_j(\phi - \mathbf{A} \cdot \mathbf{v}_j) \right), \quad (1.48)$$

The generalised momentum corresponding to coordinate x_j is

$$p_{j,x} = \frac{\partial L}{\partial \dot{x}_j} = \frac{m_j \dot{x}_j}{\gamma_j} + e_j A_x, \quad (1.49)$$

thus, the generalised momentum describes both the linear mechanical momentum and the momentum of the electromagnetic field. Via Noether's theorem, if L is independent of x_j , *i.e.* spatially homogeneous along x for particle j , then

$$\dot{p}_{j,x} = 0 \quad (1.50)$$

since

$$\frac{d}{dt} \left(\frac{\partial L}{\partial \dot{x}_j} \right) = \frac{\partial L}{\partial x_j}. \quad (1.51)$$

Consider a linearly polarised Gaussian laser pulse, with axis of polarisation along x incident on a solid target at rest. Then A_x is approximately constant along x near the beam centre². Integrating equation 1.52 and noting that initially there is no linear or electromagnetic momentum at the target, the generalised transverse momentum conservation equation for an electron in the laser field is

$$p_T = eA, \quad (1.52)$$

where p_T is the electron momentum along the polarisation axis of the laser pulse and A is the laser pulse 3-vector potential amplitude. As a sanity check, this expression complies with the ultra-relativistic similarity result of equation 1.41.

Note that this is only valid provided the electron does not radiate along the direction of polarisation as discussed by Sokolov *et al* [sokolovDynamicsEmittingElectrons2009]. The implications of *Radiation Reaction* are discussed in the following section.

1.7 QED effects

Next generation laser facilities will enable the testing of decades old theoretical predictions of Strong-Field Quantum Electro-Dynamics (SF-QED). Already Fedeli *et al* have shown in simulations that current PW-class laser facilities can access the regime using an all-optical set up based on laser-solid surface interactions [fedeliProbingStrongfieldQED2020]. The Schwinger Limit $E_S = 1.32 \times 10^{18} \text{ V m}^{-1}$ is field intensity at which the vacuum becomes non-linear. If by some means an electron can be directed towards a plane electromagnetic wave, by

²Constant relative to the scale of typical electron trajectories in such an interaction.

consideration of the Lorentz transformations of electromagnetic fields (equations ??), it is possible that provided the electron is sufficiently relativistic, in its own frame of rest it will ‘see’ electromagnetic fields intense enough to access vacuum non-linearities. The first two frontiers of SF-QED that will be accessible are Radiation Reaction and multi-photon Breit-Wheeler electron pair production. Brief introductions to these phenomena are now presented.

1.7.1 High-energy photon emission and radiation reaction

When a charged particle undergoes an acceleration, it emits electromagnetic radiation. If the electromagnetic field is sufficiently strong, *i.e.* approaching the Schwinger Limit in the rest frame of the particle, then a non-negligible fraction of the particle momentum can be transferred to the emitted high energy photon, substantially impacting the dynamics of the accelerated particle. This back reaction is known as Radiation Reaction (RR).

Smilei (detailed in the following section) implements the process of high-energy photon emission as Inverse Compton Scattering on the basis of several assumptions [nielQuantumClassicalModeling2018], namely,

1. radiating particles are ultra-relativistic and therefore radiation is emitted in the direction of travel of the particle;
2. the field varies slowly over the timescale of photon emission, this is the *locally-constant field approximation* and requires ultra-relativistic field strengths;
3. but they are small with respect to the Schwinger Limit, specifically requiring the invariants $\sqrt{c^2\mathbf{B}^2 + \mathbf{E}^2}$ and $\sqrt{c\mathbf{B} \cdot \mathbf{E}} < E_S$;
4. real particles radiated independently of their neighbours, this requires the emitted wavelength being shorter than the typical inter-particle spacing.

Provided such conditions hold, the rate of photon emission depends on two invariants [ritusQuantumEffectsInteraction1985], the electron quantum parameter

$$\chi = \frac{\gamma}{E_S} \sqrt{(\mathbf{E} + \mathbf{v} \times \mathbf{B})^2 - (\mathbf{v} \cdot \mathbf{E})^2 / c^2}, \quad (1.53)$$

where \mathbf{v} is the electron velocity and the emitted photon quantum parameter

$$\chi_\gamma = \frac{\gamma_\gamma}{E_S} \sqrt{(\mathbf{E}_\perp + \mathbf{c} \times \mathbf{B})^2 - (\mathbf{c} \cdot \mathbf{E})^2/c^2}, \quad (1.54)$$

where γ_γ is the normalised photon energy $= \hbar\omega_\gamma/m_e c^2$. The exact relationship is complex and in the the fully quantum domain ($\chi > 1$), is it not practical to solve the integrations required for all particles and instead values are extracted from precalculated tables and into a Monte-Carlo algorithm.

1.7.2 Multi-photon Breit-Wheeler pair production

Multi-photon Breit-Wheeler pair production, also known as non-linear Breit-Wheeler is the decay of a high energy photon, typically produced via RR, into an electron-positron pair in the presence of a strong electromagnetic field, explicitly,

$$\gamma + n\omega \rightarrow e^- + e^+. \quad (1.55)$$

The strength of the effect is dependent on the Lorentz invariant photon quantum parameter, equation 1.54 Cite Smilei and say, in a constant E-field, the rate of pair production increases rapidly up to $\chi_\gamma \approx 10$ at which point it saturates and slowly reduces.

1.8 Simulating the interaction

Modelling laser-plasma interactions is a notoriously challenging endeavour; due to the complexity of the many-bodied systems involved (a fully ionised centimetre cubed block of plastic contains on the order of 10^{23} particles) and the stochasticity of particle motion, it is frequently impossible to construct models *ab initio*. Instead, hydrodynamic simulation codes such as HYADES [larsenHYADESPlasmaHydrodynamics1994] and FLASH [fryxellFLASHAdaptiveMesh2000] and Particle-In-Cell simulation codes such as Smilei [derouillatSmileiCollaborativeOpensource2018], Osiris [fonsecaOSIRISThreeDimensionalFully2002] and EPOCH [bennett2017users] are used to construct phenomenological models and to direct experimentation.

1.8.1 Supercomputing resources

Modern High Performance Computing (HPC) systems are poised to enter the exascale regime ($> 10^{18}$ Floating Point Operations Per Second). With limited improvements in microprocessor technologies, such power is achieved through massive parallelisation across processing units. To enable the study of the dynamics of up to billions of macroparticles, PIC codes test the limits of current supercomputing architectures. ARCHER2, the UK's national supercomputer came online in November 2021, with it delivering over ten times the resources of its predecessor (ARCHER) [ARCHER2]. An HPE Cray EX supercomputing system with a peak performance estimated at 28 Pflops s^{-1} across 5860 nodes each with dual AMD EPYC™ 7742 64-core processor for a total of 750,080 cores, ARCHER2 was able to supply the resources required to run the costly PIC simulations for this research. The substantially cheaper HYADES simulations were performed using the Rutherford Appleton Laboratory's SCARF HPC cluster [SCARFOverview].

1.8.2 Particle-In-Cell codes

Discretisation of the Vlasov-Maxwell equations

Finding numerical solutions to the Vlasov-Maxwell equations is no straightforward task, while codes exist that are capable, such as Valis [sircombeVALISSplitconservativeScheme2009], the requirement of high resolution in both position and momentum is exceedingly costly and the use of such codes is limited with respect to their size, duration and spatial dimensions. A more tractable approach is to discretise the distribution function into N_s *quasi-particles*³. These are often referred to as *macro-particles* in practice and typically represent a large number of real particles, such that

$$f_s(t, \mathbf{x}, \mathbf{p}) = \sum_{p=1}^{N_s} w_p S(\mathbf{x} - \mathbf{x}_p(t)) \delta(\mathbf{p} - \mathbf{p}_p(t)), \quad (1.56)$$

where w_p is the quasi-particle's weight, \mathbf{x}_p and \mathbf{p}_p are its position and momentum respectively, δ is the Dirac-delta distribution and $S(\mathbf{x})$ the shape-function

³Originally introduced by Langdon and Birdsall as *clouds* [langdonTheoryPlasmaSimulation1970].

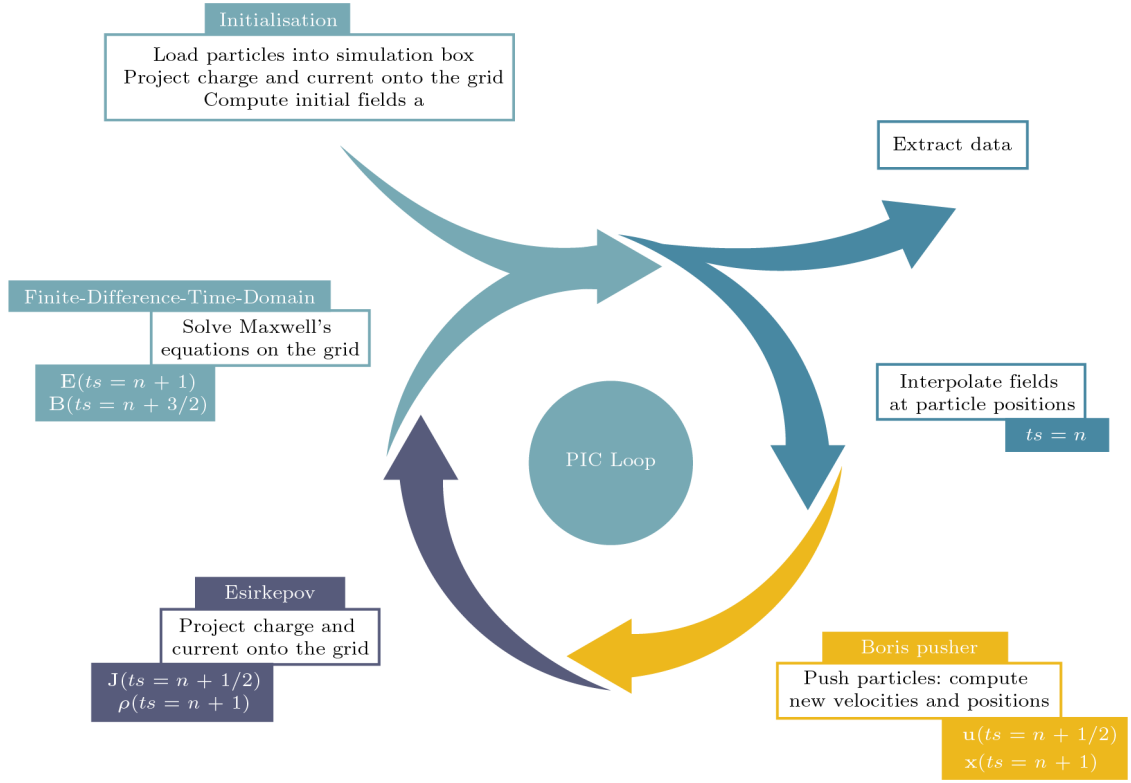


Figure 1.3: A schematic of the PIC code loop and the algorithms performed from time step, ts , from n to $n + 1$.

chosen to represent the quasi-particle. The Vlasov equation is then integrated along the continuous trajectories of the quasi-particles while Maxwell's equations are solved on a discrete spatial grid of *cells*. Such a code is aptly named a *Particle-In-Cell* (PIC) code. A schematic of the standard PIC code algorithm is presented in figure 1.3. After particle and field initialisation, fields are interpolated at particle positions. The well-established momentum-conserving *Boris pusher* algorithm computes the new macro-particle velocities and positions [borisRelativisticPlasmaSimulationoptimization1970]. Particles are advanced in time using a *leap-frog* scheme, where positions are defined at integer, n , time steps and momenta at half integer, $n + 1/2$. The charge conserving Esirkepov algorithm [esirkepovExactChargeConservation2001] projects the new charge and current densities onto the grid to then solve Maxwell's equations on the grid using the Finite-Difference-Time-Domain approach [tafloveComputationalElectromagneticsFinite]. To ensure space and time centering of the electromagnetic field derivatives in

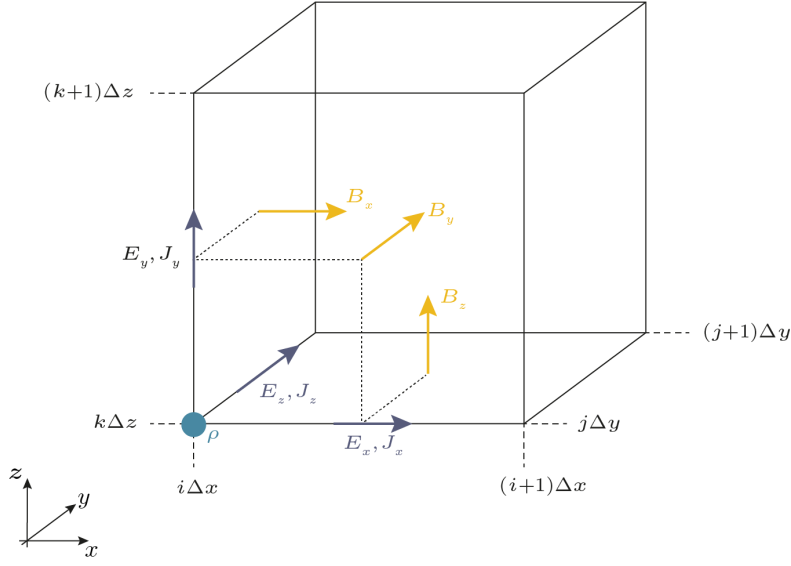


Figure 1.4: A representation of the staggered 3D Yee grid for the cell at $(i\Delta x, j\Delta y, k\Delta z)$ for spatial centering of the curl operations, including the locations where all system properties are defined.

Maxwell's equations, electric and magnetic fields are discretised on the staggered *Yee grid* as represented in figure 1.4. with electric fields defined at integer time steps and magnetic fields at half-integer time steps.

Smilei

Smilei (for Simulating Matter Irradiated by Light at Extreme Intensities) is a modern collaborative, massively-parallel, fully relativistic and open source plasma physics PIC code and the major workhorse for this thesis⁴. Produced by M. Grech's team(CHECK THIS) at École Polytechnique [**derouillatSmileiCollaborativeOpensource2018**], its recent development was motivated by the rapid advancements of multi-petawatt facilities both globally and locally with the recent completion of the 10 PW Apollon laser facility and by the availability of supercomputing power which has 'skyrocketed' in recent years [**derouillatSmileiCollaborativeOpensource2018**]. Indeed, the 3D Particle-In-Cell (PIC) simulations discussed in this thesis required the parallelisation of almost 20 % of the computing resources available on ARCHER2.

⁴At points benchmarks against the EPOCH and Osiris PIC codes were performed.

Units of	SI units	Normalisation
velocity	m s^{-1}	c
charge	C	e
mass	kg	m_e
momentum	kg m s^{-1}	$m_e c$
energy/temperature	J	$m_e c^2$
time	s	ω_L^{-1}
length	m	c/ω_L
number density	m^{-3}	n_c
electric field	V m^{-1}	$m_e c \omega_L / e$

Table 1.2: Smilei normalisations for common quantities with the laser angular frequency ω_L set at the reference angular frequency.

Reference units

Given the broad range of magnitudes linked to multi-petawatt and femtosecond laser pulses, solid density plasmas, micrometer wavelengths, and attosecond electron bunches, it becomes significantly more convenient to transform them into dimensionless normalised values. Smilei operates in such units. This normalisation is not chosen *a priori*, instead results can be scaled by an arbitrary reference angular frequency. This is extremely useful when working with boosted frames of reference. As this thesis focuses on the interaction of a laser pulse with plasma, the laser pulse angular frequency, ω_L is set as the frequency of reference. A list of the most common normalisations are given in table 1.2.

Simulation parameters

Silver-Müller boundary conditions for the simulation box edges [**barucqAsymptoticBehaviorSol**] are able to absorb and inject electromagnetic waves and particles. Note that there can be non-physical reflection of electromagnetic waves at such boundaries leading to some error.

The quasi-particle shape function $S(\mathbf{x})$ determines the projection of particle charge onto the grid. It is symmetric in all dimensions with respect to \mathbf{x} and

extends over n cells of width Δx in each direction where n is the interpolation order. It can be written as a product across D dimensions,

$$S(\mathbf{x}) = \prod_{\mu=1}^D s^{(n)}(x^\mu). \quad (1.57)$$

Smilei implements orders 2, 3 and 4, the explicit shape functions are

$$s^2(n) = \begin{cases} \frac{1}{\Delta x} \left(1 - \left|\frac{x}{\Delta x}\right|\right) & \text{if } |x| \leq \Delta x, \\ 0 & \text{otherwise,} \end{cases} \quad (1.58a)$$

$$s^3(n) = \begin{cases} \frac{3}{4\Delta x} \left(1 - \frac{4}{3} \left(\frac{x}{\Delta x}\right)^2\right) & \text{if } |x| \leq \frac{1}{2}\Delta x, \\ \frac{9}{8\Delta x} \left(1 - \frac{2}{3} \left|\frac{x}{\Delta x}\right|\right)^2 & \text{if } \frac{1}{2}\Delta x < |x| \leq \frac{3}{2}\Delta x, \\ 0 & \text{otherwise,} \end{cases} \quad (1.58b)$$

$$s^4(n) = \begin{cases} \frac{2}{3\Delta x} \left(1 - \frac{3}{2} \left(\frac{x}{\Delta x}\right)^2 + \frac{3}{4} \left|\frac{x}{\Delta x}\right|^3\right) & \text{if } |x| \leq \Delta x, \\ \frac{4}{3\Delta x} \left(1 - \frac{1}{2} \left|\frac{x}{\Delta x}\right|^3\right) & \text{if } \Delta x < |x| \leq 2\Delta x, \\ 0 & \text{otherwise.} \end{cases} \quad (1.58c)$$

While the correct implementation of collisions in PIC codes remains an open problem [**Collisions**], Smilei has implemented relativistic binary collisions between macroparticles using a Monte-Carlo based scheme [**perezImprovedModelingRelativistic2012**]. The aforementioned QED processes of Inverse Compton scattering and non-linear Breit-Wheeler pair production are included using the built-in Smilei packages [**derouillatSmileiCollaborativeOpenSource2018**]. These processes can lead to cascades of many particles being added to the simulations. Macroparticle merging can increase simulation efficiency and reduce the memory footprint. Smilei implements such a scheme, inspired by that designed by Vranic *et al* [**vranicParticleMergingAlgorithm201**] that is computationally efficient and conserves energy, momentum and charge within a cell. While Smilei contains modules to handle ionisation, with reference to figure 1.1 these are deemed unnecessary for the laser intensities considered in this thesis.

Parallelisation in practice

In the following discussion, where differences in language occur, objects are given as their ARCHER2 (Smilei) names. The Smilei simulation box consists of a grid of cells as in figure 1.5. The box is decomposed into *patches* consisting of many cells. Patches

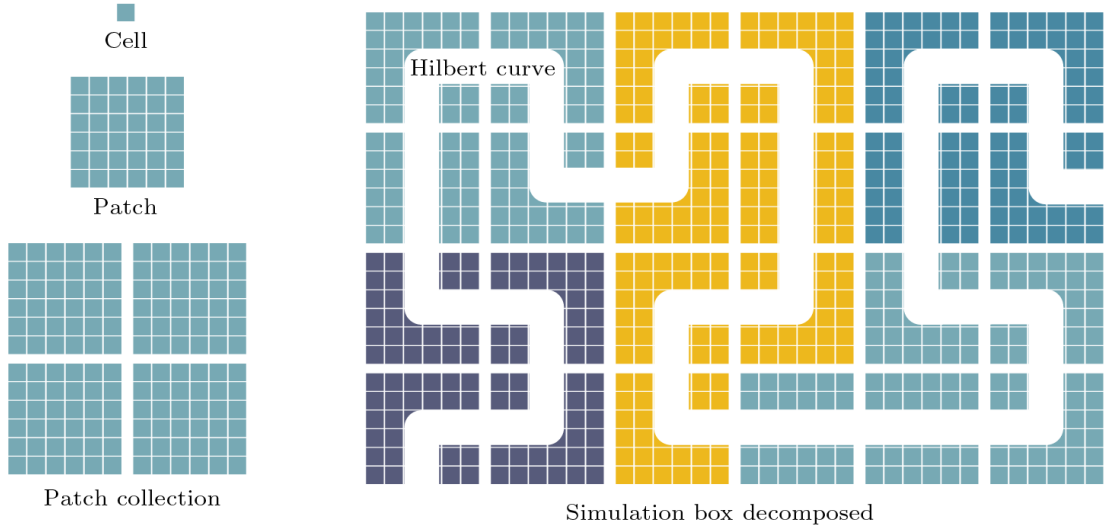


Figure 1.5: Smilei simulation box decomposition into cells, patches and MPI patch collections. Cells are grouped into patches, patches are grouped into MPI patch collections. MPI patches are assigned contiguously along the Hilbert curve.

are arranged into *MPI patch collections* assigned contiguously along a Hilbert curve.

Archer consists of many *CPUs (cores)* that can each perform computational tasks. CPUs are grouped together into *nodes*. Memory is shared within a node such that all CPUs (cores) in a node can operate on the same data. When optimised, ARCHER2's memory in each node is split into 8 *sockets*. These 8 sockets each perform a *task (MPI process)*. Each task (MPI process) has 16 CPUs (cores) assigned that each perform a *thread*. A thread is a sequence of instructions from the program.

Each task (MPI process) handles one *MPI patch collection*. Threads work through patches. Figure 1.6 represents this division of labour. Threads do not need to wait for other threads in their process to tackle new patches in their MPI patch collection. This is a form of local *dynamic load balancing*. If an MPI patch collection is overloaded, a patch is offloaded to a contiguous MPI patch collection.

There are several considerations for simulation optimisation. Tasks (MPI processes) should always be assigned more patches than threads. To apply the Hilbert curve, it is necessary that the number of patches in each dimension is a power of 2. The less cells in a patch, the more efficient the load balancing, however, the cost of synchronisation between patches increases, although generally the gain in efficiency from load balancing by increasing patch number will win out

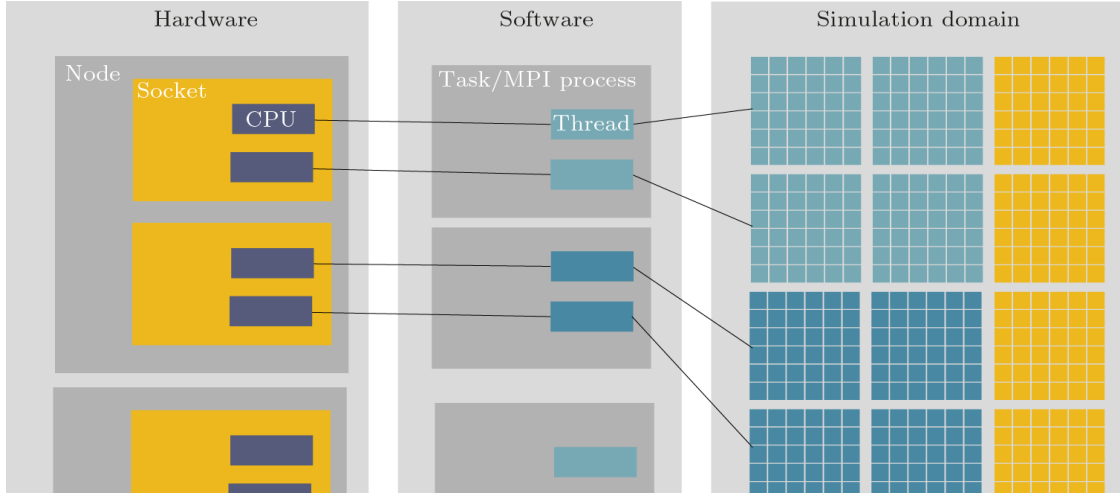


Figure 1.6: Representation of the interaction of the ARCHER2 hardware and software components when running Smilei. Each CPU is assigned a thread, each task is carried out by one socket. A task tackles one MPI patch collection with threads working through patches.

at later times with increasing efficiency for increased frequency of load balancing [derouillatSmileiCollaborativeOpensource2018]. Note that smaller patches are preferable when there are small regions with large numbers of particles, as in laser-solid surface interactions, however, the minimum patch size is dependent on the shape function of the macro-particles.

Sources of error inherent to PIC codes

Despite their relatively intuitive interpretation, PIC codes are famously finicky and prone to errors, most notably that of numerical self heating⁵. There are three conditions required for stability.

To ensure stability, or at least to minimise instability, there are several conditions which must be met. Naturally, the time step, Δt , and cell size ($\Delta x \Delta y \Delta z$) must adequately capture all interesting features of a given simulation. Typically such features are plasma wave oscillations,

$$\Delta t \omega_p \ll 1, \quad (1.59)$$

⁵Standard PIC code algorithms are charge and momentum conserving but not energy conserving [derouillatSmileiCollaborativeOpensource2018].

and laser pulse electromagnetic field oscillations or higher order harmonics of the laser pulse if that is of interest, for the n th harmonic

$$\Delta t \omega_L n \ll 1. \quad (1.60)$$

Note this also ensures that macroparticles are smaller than the wavelengths of the system, a requirement to ensure they mimic real particles [okudaCollisionsPlasmaFiniteSize1970]

Relativistic PIC codes must satisfy the much-acclaimed [demouraCourantFriedrichsLewy2013]

Courant-Friedrichs-Lewy condition,

$$\frac{1}{c\Delta t} > \sqrt{\frac{1}{(\Delta x)^2} + \frac{1}{(\Delta y)^2} + \frac{1}{(\Delta z)^2}}, \quad (1.61)$$

thus preventing light and relativistic particles from crossing a cell in one timestep and generating numerical Cerenkov radiation [birdsall2004plasma]. As with real plasmas and real particles, to avoid numerical charge fluctuation and ensure collective behaviour of macroparticles,

$$\frac{4}{3}\pi\lambda_D^3 n_{\text{macro}} = N_{D,\text{macro}} \gg 1, \quad (1.62)$$

where n_{macro} is the macroparticle density [birdsall2004plasma]. To avoid numerical heating, the cell size must resolve the Debye length,

$$\frac{\lambda_D}{\Delta x} \geq 1, \quad (1.63)$$

failure to do so may cause plasma self-heating until the Debye length matches the cell size [birdsall2004plasma]. Interestingly, Brackbill *et al* [brackbillEnergyMomentumConser] observed in their simulations that setting $\lambda_D/\Delta x = 1$ was most effective at reducing spurious heating. Arber *et al* [arberContemporaryParticleincellApproach2015] performed extensive simulations exploring this instability. If the Debye length is not resolved, after an initial period of rapid self-heating, the temperature increases linearly and can be modelled as

$$\frac{dT_{\text{eV}}}{dt_{\text{ps}}} = \alpha_H \frac{n_{23}^{3/2} \Delta x_{\text{nm}}^2}{N_{\text{ppc}}}, \quad (1.64)$$

where T_{eV} is the temperature in electron volts, t_{ps} is the time in picoseconds, n is the plasma electron number density in units of 10^{23} cm^{-3} , Δx_{nm} is the cell size in

nanometres and N_{ppc} is the number of macroparticles per cell with α_{H} , the heating coefficient, determined from their simulations. For a top-hat macroparticle shape function they found $\alpha_{\text{H}} = 3000$ with an order of magnitude reduction for every increase in order of the shape function and further improvements from using current smoothing techniques. Note that the heating curves are roughly self similar at all points and thus while equation 1.64 was established in the linear regime only, its scalings remain useful to compare simulations at all times.

The final instability that shall be discussed is the *finite grid instability*. This is the aliasing error associated with particles properties being deposited at grid points. Is most catastrophic for cold drifting plasmas and depends on the *beam Debye length*,

$$B = \frac{u}{\omega_p \Delta x}, \quad (1.65)$$

where u is the beam speed. While their theory predicts stability for $B > 0.25$, Brackbill *et al* [**brackbillEnergyMomentumConservation2016**] observed instability growth for all beam temperatures in their simulations, although they found the percentage error is a small fraction for $B > 10$.

2

Attosecond X-ray harmonics on the ORION laser facility

Contents

2.1	A plan	29
2.2	Theory	30
2.2.1	The ROM model	30
2.2.2	The normalisation factor	30
2.2.3	Hole boring	31
2.3	Experimental data processing	36
2.3.1	Image plate calibration	36
2.3.2	OHREX calibration	38
2.3.3	Extracting the data	39

2.1 A plan

This chapter reports on the March 2023 experiment at the ORION laser facility, AWE, Aldermaston. The UK's most powerful sub-picosecond laser.

Important sections include: HYADES scale length sims, ORION parameters and description of the setup, targets etc, data analysis after, beamlet sims, HHG theory

I think the appropriate order would be theory, simulation, experiment layout, data analysis since then I can use all things inferred from theory and simulation

to justify the data analysis. It also means ending well.

The early developments in the field are outlined by Teubner *et al* [teubnerHighorderHarmonicsLa

HHG from solids has demonstrated significantly higher conversion efficiencies than for HHG from gases nor are there any limitations to the applied laser intensity [teubnerHighorderHarmonicsLaserirradiated2009]. SHHG has thus been a field of huge interest over the past three decades for the production of bright coherent attosecond harmonics.

2.2 Theory

2.2.1 The ROM model

Apply Bourdier method and conservation of generalised momentum, we see that

and thus non-linearity

and thus the thing we need to solve is blah.

The laser pulse leads to macroscopic oscillation of the plasma surface and therefore a corresponding oscillation of the ARP. One can understand this leading to a sub cycle Doppler shift in the reflected pulse. These pulses of radiation separated by the laser pulse frequency must therefore in the spectral domain consist of HH.

The Relativistic Oscillating Mirror (ROM) model describes an extension.

The following outlines the key ideas

Ok: assume I have the expression from Baeva's paper (do this tomorrow)

2.2.2 The normalisation factor

Baeva's theory provides us with the relative intensity of harmonics. However, for comparison with the absolute spectral intensity of harmonics in experiment, the normalisation factor is required. This can be calculated from conservation of energy. For arbitrary harmonic order scaling, n^{-p} , the spectral intensity of the harmonic beam is

$$I_\omega(\omega) = \frac{dE_\omega(J)}{dAd\omega} = I_0 \sum_{n=1, \text{ odd}}^{n_C} n^{-p} S_n \left(\frac{\omega}{\omega_L} - n \right) \quad (2.1)$$

up to the cutoff, n_C . Here $S_n(\omega/\omega_L - n)$ is the spectral shape function of the n^{th} harmonic in reciprocal space and I_0 is the normalisation factor of interest. From conservation of energy,

$$\int I_\omega(\omega) d\omega dA = ER, \quad (2.2)$$

where E the total energy of the laser pulse and R is the reflectivity of the Relativistic Plasma Mirror (RPM). Intuition suggests the spectral shape function for the n^{th} harmonic retains the spectral shape of the incident laser pulse, *i.e.* for a laser pulse with a Gaussian temporal profile, this corresponds to a Gaussian centred at $n\omega_L$ of width $\sigma_L = 1/t_L$, where t_L is the laser pulse width. Simulations show this is a reasonable approximation.

Simulations also show that for the SP1 laser, the incident laser pulse significantly suppresses the even harmonics, hence,

$$ER = \int_0^\infty I_0 \sum_{n=1, \text{ odd}}^{n_C} n^{-p} e^{-(\omega/\omega_L - n)^2/\sigma_L^2} d\omega. \quad (2.3)$$

The integral and summation order can be reversed. Since $\sigma_L \ll \omega_L$, all integrals in the summation are $\approx \int_{-\infty}^\infty$ and therefore,

$$ER \approx I_0 \sum_{m=0}^{n_C/2-1} (1+2m)^{-p} \sqrt{\pi} \sigma_L \omega_L, \quad (2.4)$$

thus,

$$ER \approx I_0 \sqrt{\pi} \sigma_L ((1-2^{-p})\zeta(p) - 2^{-p}\zeta(p, \frac{n_C+1}{2})), \quad (2.5)$$

where $\zeta(p)$ and $\zeta(p, (n_C+1)/2)$ are the Riemann Zeta and Hurwitz Zeta functions respectively. The final term can be neglected for a petawatt class laser pulse where $n_C \gg 1$. In the case of an ideal p -polarised laser pulse,

$$ER \approx I_0 \sqrt{\pi} \sigma_L \zeta(p). \quad (2.6)$$

For the ROM regime, $p = 8/3$ and the RPM is extremely efficient, $R \approx 1$. Thus, I_0 can be estimated from the system parameters.

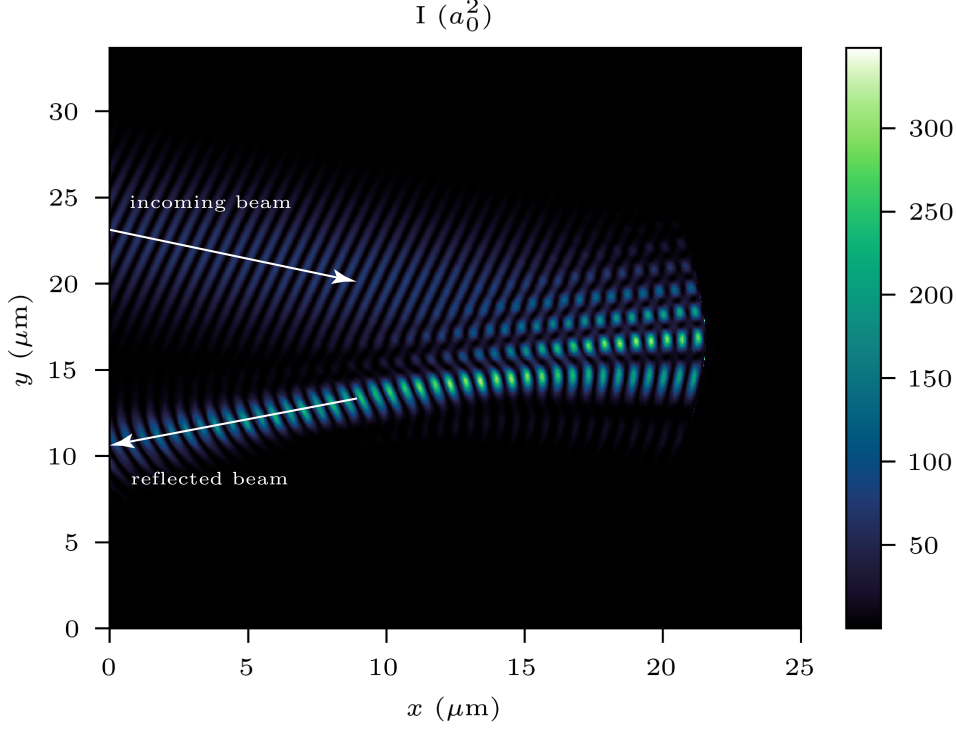


Figure 2.1: Electromagnetic field intensity in a 2D PIC simulation of a relativistic ($a_0 = 30$) laser pulse incident on a solid density plasma. The incoming beam is specularly reflected off the target which is curved by the radiation pressure leading to beaming in the reflected harmonic beam.

2.2.3 Hole boring

As observed in the ZVP plots, on long timescales relative to the laser pulse cycles, via the ponderomotive pressure of the laser, the plasma front moves inwards. This is hole boring [1]. One can derive a hole boring velocity by considering conservation of momentum in this quasi-static state. Since the hole boring velocity is laser pulse intensity dependent, the spatial profile of the laser will be imprinted on the surface. Typically Gaussian in shape, for high power laser systems, this can to first order generate a focusing RPM and a beaming of the specularly reflected signal, as in Figure 2.1. To access the highest possible electromagnetic field intensities, the laser pulse is focused on target to the diffraction limit. However, since the diffraction limit scales linearly with the wavelength, higher-order harmonics can be refocused to a smaller spot via this mechanism allowing access to unprecedented peak intensities.

Vincenti *et al* demonstrated intensity gains of over 1000 with currently accessible parameters in three-dimensions (3D) PIC simulations [2], suggesting a realistic route to the Schwinger Limit using next-generation laser facilities. Regardless of any blue-skies purposes, it is clear any prediction of High Harmonic Generation (HHG) beam intensity must account for hole boring and is therefore an essential component of the ORION experiment analysis.

Applying momentum balance between the laser pulse and particles in the rest frame of the RPM surface, the hole boring velocity is

$$\frac{v_{\text{HB}}}{c} = \sqrt{\frac{R \cos \theta}{2} \frac{Z m_e}{A m_p} \frac{n_c}{n_e(x_i(t, y))}} a_L(t, y) = \Pi a_L(t, y), \quad (2.7)$$

where R is the RPM reflectivity, θ is the angle of incidence, 16° in the ORION experiment, Z and A are the atomic and atomic mass numbers respectively for the plasma ions, n_c is the plasma critical density, $n_e(x_i(t, y))$ the electron number density and $x_i(t, y)$ the depth of hole boring, from the Supplementary Material [3]. For the ORION laser pulse parameter space $\Pi \ll a_L \forall t$, *i.e.* we are in the relativistic electron and non-relativistic ion regime. Hence, the relativistic correction derived by Robinson *et al* [4] to Equation 2.7 can be neglected. Due to the high contrast and long duration of the ORION beamlines, there is minimal pre-plasma formation on the front surface and therefore the number density is simply the number density of the material in solid form and n_e is independent of $x_i(t, y)$. Robinson *et al* [5] generalised momentum conservation to multiple species, simply replace the mass density with the composite mass density $\rho = \sum_j m_{ij} n_{ij}$, then

$$\frac{A n_e}{Z} \rightarrow \sum_j \frac{A_j n_{ej}}{Z_j}, \quad (2.8)$$

where n_{ej} is the number density of electrons that originated from the j ion.

The spatio-temporal envelope of the normalised vector potential of the laser pulse incident on the target surface is modelled as

$$a_L(t, y) = a_0 e^{-\frac{y^2}{2w_L^2}} g(t - t_0) \quad (2.9)$$

where w_L is the beam waist on target and $g(t)$ the temporal envelope, a Gaussian or sech profile and t_0 the main pulse peak time.

Integrating equation 2.7,

$$x_i(y) = \int v_{\text{HB}} dt = \Pi \int_{-\infty}^t a_L(t, y) c dt. \quad (2.10)$$

At the peak of the main pulse,

$$x_i(y) = \Pi a_0 c e^{-\frac{y^2}{2w_L^2}} G, \quad (2.11)$$

where $G = \int_{-\infty}^{t_0} g(t - t_0) dt \sim t_L$ and t_L is the laser pulse temporal width.

The total denting is a combination of the peak electron-ion charge separation, x_e (which leads to the intrinsic phase imprint on the HHG beam) and equation 2.10. Note that for the long pulse duration of the ORION laser, $x_i \gg x_e$ and therefore x_e can be neglected.

Applying a Taylor expansion to the spatial profile of equation 2.10 around the laser spot centre,

$$x_i = \text{constant} - \frac{y^2}{4f_p} + \mathcal{O}(y^4), \quad (2.12)$$

where, to first order, this is the equation of a parabolic mirror with focal length

$$f_p(t) = \frac{w_L^2}{4\Pi a_0 c G}. \quad (2.13)$$

Following the Vincenti *et al* derivation [3], the denting parameter is defined as,

$$\delta_T = x_i|_{(y=0)} - x_i|_{(y=\sqrt{2}\omega_L)}. \quad (2.14)$$

Hence,

$$\delta_T = \frac{w_L^2}{2f_p} = 2\Pi a_0 c G, \quad (2.15)$$

and is independent of laser focal spot size.

If the spatial profile of the n^{th} harmonic beam can be adequately described by a Gaussian at the plasma mirror plane, with a beam width described by the harmonic source size, w_n ,

$$h_n \sim e^{-r^2/w_n^2}, \quad (2.16)$$

then the beam profile is known at all distances, z from the target. Its divergence, defined as

$$\theta_n = \lim_{z \rightarrow \infty} \frac{w_n(z)}{z}, \quad (2.17)$$

is therefore

$$\theta_n = \theta_n^0 \sqrt{1 + \Psi_n^2}, \quad (2.18)$$

where $\theta_n^0 = \lambda_n / \pi w_n$ is the harmonic divergence in the absence of RPM denting and

$$\Psi_n = \frac{2\pi}{\cos \theta} \left(\frac{w_n(0)}{w_L} \right)^2 \frac{\delta_T}{\lambda_n} \quad (2.19)$$

is the dimensionless focusing parameter. If $\Psi_n \gg 1$, as is true for the short wavelength X-ray harmonics of interest,

$$\theta_n \approx \frac{w_n(0)}{f_p \cos \theta} \quad (2.20)$$

and the divergence is dominated by RPM curvature.

Far from focus, at the detector plane $z = 2.4$ m from the target,

$$w_n \approx z \tan \theta_n. \quad (2.21)$$

The corresponding magnification factor at detection is thus

$$\gamma_n(z) = \frac{w_n(z)}{w_n(0)}, \quad (2.22)$$

thus the laser intensity at detection is reduced by a factor $\gamma_n(z)^{-2}$.

At large distances,

$$\gamma_n \approx \frac{z \tan(w_n(0)/(f_p \cos \theta))}{w_n(0)} \quad (2.23)$$

Taking the Taylor expansion of the tangent, one sees that the magnification factor is only weakly dependent on the harmonic source size (f_p is independent of the source size), whereas the magnification is strongly dependent on the the laser spot size ($\sim w_L^4$).

At the new RPM focal point, $z = z_f$, the demagnification factor is [3]

$$\gamma_n(z_f) = \frac{1}{\sqrt{1 + \Psi_n^2}}, \quad (2.24)$$

this determines the new peak intensity accessible via hole boring.

2.3 Experimental data processing

2.3.1 Image plate calibration

Image plates (IPs) are reusable recording media that detect ionising radiation and are particularly suitable for the detection of X-rays produced in laser-plasma interactions. Their response is well understood and their sensitivities to a wide spectrum photon energies have been absolutely calibrated on the ORION facility [6]. Albeit for the FLA3000 scanner not the FLA7000 used in this experiment. However, the deviation in response is negligible for the photon energies measured. In this experiment the Fuji Biological Analysis System (BAS) TR-type IPs were used. They have a phosphor layer composed of $\text{BaFBr}_{0.085}\text{I}_{0.15}$ with density 2.61 g cm^{-3} and thickness $60 \mu\text{m}$ but no mylar layer. This makes them suitable for low energy X-ray detection. When scanned, the IP releases blue photons via photostimulated luminescence (PSL), which is then collected by a photomultiplier tube. The PSL value is generalised across scanner types from the measured ‘Grey’ (G) value by

$$\text{PSL} = (0.23284G^2 \times 10^{-9}) \left(\frac{\Delta x}{100} \right)^2 W \times 10^{-L/2}, \quad (2.25)$$

where Δx is the scanner resolution ($= 25 \mu\text{m}$ in this experiment), L is the latitude parameter, and

$$W = 0.092906 + 1370.8e^{-0.014874V} + 654.24e^{-0.011026}, \quad (2.26)$$

where V is the scanner voltage [7].

IP photon sensitivity, ψ , the number of PSLs per incident photon, is dependent on photon energy. Meadowcroft *et al* modelled this as,

$$\psi_j = \eta(m_j h\nu + c_j), \quad (2.27)$$

where $h\nu$ is the photon energy and m_j and c_j are linear fit parameters valid for specific energy ranges, j . For the Fuji BAS TR-type IP and for X-rays in the range 0-6.0 keV, $m_j = 0.54(5) \text{ mPSL keV}^{-1}$ and $c_j = 0.020(2) \text{ mPSL}$. The IP absorption efficiency in mPSL per photon is

$$\eta(h\nu, T_i, T_s) = \exp(-n_i \Phi_i(h\nu) T_i) [1 - \exp(-n_s \Phi_s(h\nu) T_s)], \quad (2.28)$$

where n is the layer density, $\Phi(h\nu)$ is the total cross-section of the layer, T the effective layer thickness, s and i correspond to the sensitive (phosphor) and insensitive (mylar) layers of the IP respectively [8]. The first term is neglected in the absence of an insensitive (mylar) layer in TR-type IP. Below 50 keV, the dominant mode for X-ray absorption into the IP is the photo-electric effect, where

$$\Phi_{\text{ph}} \approx 3 \times 10^{12} \frac{Z^4}{(h\nu)^{3.5}} \quad (2.29)$$

and Z is the atomic number [9] and Φ_{ph} is given in units of Barn per atom. At 2.4 keV, that corresponds to a sensitivity of 1.32 mPSL per incident photon.

It is generally inevitable that some time will elapse between laser shot and IP scan. For this experiment 30 minutes was typical, in which time some fading of the IP occurs that must be accounted for. IP fading can be modelled as an attenuation factor,

$$F(t) = A \exp(-t/\tau) + B, \quad (2.30)$$

where t is the time between shot and scan and A , τ and B are found from fits to experimental data. A key aspect of the exponential decay is that the attenuation depends only on the signal at that moment in time and not the initial conditions. This has been shown to be true in experiment [6].

At 20°C at the ORION facility *Meadowcroft et al* [6] determined that for the Fuji BAS TR-type IP, the optimum fit for the parameters of equation 2.30 is $A = 0.347(22)$, $B = 0.693(11)$ and $\tau = 35.5(53)$ minutes. Therefore at 30 minutes, $F(t) = 0.84$.

In summary, the number of PSL measured on an IP can be converted to an incident number of photons via

$$N(h\nu) = \frac{\text{PSL}}{F(t)} \frac{10^3}{\psi(h\nu)} = P(h\nu) \text{PSL}. \quad (2.31)$$

Crystal	Range, $n = 1$ (eV)	Range, $n = 2$ (eV)
KAP (100)	585-625	1170-1245
Quartz ($10\bar{1}0$)	1830-1950	3660-3900
Quartz ($10\bar{1}1$)	2330-2480	4660-4960

Table 2.1: Photon energy ranges captured by the three lowest energy OHREX crystals when operating at their nominal central Bragg angle of 51.3° for first and second diffraction orders, n .

2.3.2 OHREX calibration

The Orion High REsolution X-ray spectrometer (OHREX), housed on the ORION laser target chamber outer wall, utilises a spherically bent crystal geometry to spatially focus and spectrally analyse photons from the target chamber [10] with a high signal-to-noise ratio. The measured signal has been absolutely calibrated for a range of energies using a variety of crystals [11]. The OHREX can hold two crystals at a time. At each crystal’s spatial focal plane a two-dimensional image is formed, one dimension is spatial, the other spectral. The energy range accessed by a given crystal is determined by the crystal rotation but all OHREX crystals are designed for operation at a nominal central Bragg angle of $\theta_B = 51.3^\circ$ with the corresponding wavelength determined from Bragg’s Law, $n\lambda = 2d \sin \theta_B$, for the appropriate crystal plane. The range around that central photon energy is determined by the crystal width in the spectral dimension.

MacDonald *et al* determined a quadratic fit for each crystal’s dispersion relation to connect position along the image to photon energy [11]. Unfortunately in this experiment, the image lengths varied from those in the previous experiment, a likely consequence of slight defocusing of the optic. Note that the OHREX geometry is designed such that precise focus is not necessary to achieve good results [10].

Instead, a simple linear dispersion relation based on the known maximum and minimum energies accessed by the crystal was applied across the crystal images, a reasonable approximation to the dispersion relation determined by MacDonald *et al* [11] (the quadratic correction is small). The energy ranges for the three lowest energy OHREX crystals are given in table 2.1.

Provided full illumination of the 6 cm \times 4 cm crystal, the spatial dimension can be safely integrated over to calculate the measured signal, $M(h\nu)$ in J mm $^{-1}$ and remove uncertainty from the IP drifting from the ideal focal plane. (In this experiment we assume that the harmonic beam width at the crystal position is larger than the size of the crystal, a reasonable assumption since beam divergence $\approx 10^\circ$ and the 6 cm \times 4 cm crystal sits 2.4 m from the target.). This corresponds to a source spectral intensity incident on the crystal $S(h\nu)$ measured in J keV $^{-1}$ sr $^{-1}$ via the spectrometer response, $G(h\nu)$, explicitly,

$$M(h\nu) = S(h\nu)G(h\nu). \quad (2.32)$$

The absolute throughput of the crystals was measured by MacDonald *et al* in a previous ORION experiment and fit parameters for

$$G(h\nu) = A(h\nu)^2 + B(h\nu) + C, \quad (2.33)$$

where $(h\nu)$ is the photon energy measured in eV, determined for both p- and s-polarised incident light and for first and second diffraction orders [11]. The parameters for the lowest few energy crystals are presents in Table 2.2. There is unfortunately no spectrometer response data for the 10 $\bar{1}$ 0 crystal to first order due to the Si K edge sitting within the energy range and the dramatic effect this has on absorption in its vicinity [12].

The OHREX is equipped with a 50 μ m Beryllium filter to protect the crystals. The corresponding signal attenuation can be calculated using X-ray transmission data [13].

2.3.3 Extracting the data

The quartz OHREX crystals 10 $\bar{1}$ 0 and 10 $\bar{1}$ 1 were fielded on the experiment. Crystal images were recorded with BasTR2040 Fuji Image Plate. A typical shot image scanned with the FLA7000 scanner and converted to photostimulated luminescence units (PSLs) is given in figure 2.2. The average background signal was subtracted. The x - and y -axes were converted from pixels to to mm using the scanner resolution,

Crystal	Order	Polarisation	A	B	C
KAP (100)	1	s	1.72×10^{-15}	-4.69×10^{-12}	2.89×10^{-9}
		p	1.40×10^{-14}	-1.74×10^{-11}	5.42×10^{-9}
	2	s	3.64×10^{-16}	-9.64×10^{-13}	6.95×10^{-10}
		p	5.03×10^{-10}	8.09×10^{-13}	5.03×10^{-10}
Quartz (10 $\bar{1}$ 0)	1	s
		p
	2	s	4.50×10^{-15}	-3.40×10^{-11}	6.52×10^{-8}
		p	1.13×10^{-15}	-8.86×10^{-12}	1.73×10^{-8}
Quartz (10 $\bar{1}$ 1)	1	s	1.00×10^{-16}	-1.74×10^{-12}	4.93×10^{-9}
		p	2.78×10^{-15}	-1.41×10^{-11}	1.79×10^{-8}
	2	s	4.70×10^{-16}	-4.50×10^{-12}	1.11×10^{-8}
		p	2.10×10^{-16}	2.11×10^{-12}	5.30×10^{-9}

Table 2.2: Sensitivity fit parameters as a function of photon energy, $h\nu$ in electron-volts ($G(h\nu) = A(h\nu)^2 + B(h\nu) + C$) for the three lowest energy OHREX crystals for p- and s-polarised incident photons and first and second diffraction orders [11]. Note that no data is available for the first order of the quartz (10 $\bar{1}$ 0) crystal.

Figure 2.2: Unprocessed shot data from a FLA7000 scanned image plate converted to PSLs. The image plate and two crystal images are clearly visible.

($25 \mu\text{m px}^{-1}$) and then energies using the appropriate dispersion relations. The data was then integrated over y to obtain the intensity in units of PSL mm^{-1} across each crystal image. Then the corresponding source signal is

$$S(h\nu)[\text{J keV}^{-1} \text{sr}^{-1}] = \frac{d\text{PSL}}{dx} \frac{P(h\nu)}{G(h\nu)} h\nu, \quad (2.34)$$

which can then be converted to a measured spectral intensity per harmonic at distance $r = 1$ from the source, ready to be directly compared to the theory,

$$I_n^{\text{meas}}|_{(r=1\text{ m})} = S(h\nu) \frac{dh\nu(\text{keV})}{dn}. \quad (2.35)$$

No sensitivity data is available for the 10 $\bar{1}$ 0 quartz crystal, instead this lower energy crystal was fielded to attempt resolving of the X-ray harmonics. At the experiment planning stage it was unknown if this would be possible. Now that the simulations have been performed, we know that the non-optimal ORION

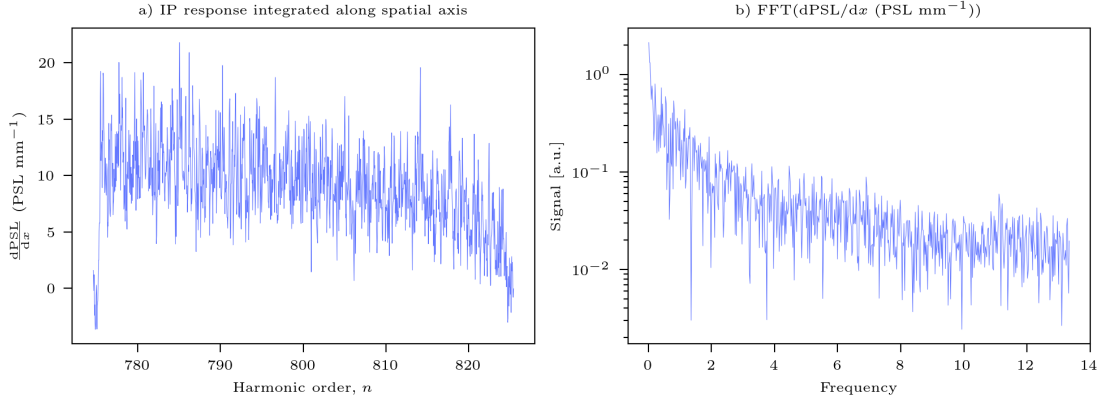


Figure 2.3: Typical (SP1, PMMA) uncalibrated shot data for the quartz ($10\bar{1}0$) image a) IP spatial axis integrated signal with dispersion axis. b) Fourier transform of a) with no evidence of harmonics.

target chamber geometry leads to merging of the harmonics even before the water window at 282 eV. This is consistent with the findings, Figure 2.3 is a typical integrated signal in PSLmm and the corresponding Fourier transform for the quartz ($10\bar{1}0$) crystal image.

Calibration and polarisation

The choice of the spectrometer response function, $G(h\nu)$, is non-trivial. One must firstly be assured that the second order contribution is small relative to the first, true for this source spectrum. And also think carefully about the anticipated polarisation in the OHREX interaction plane. The OHREX response to p-polarised light is approximately an order of magnitude lower than for s-polarised light. From Figure X we are assured that only the p-polarised (with respect to the target interaction plane) X-rays are specularly reflected to the OHREX. Corresponding polarisation out of the OHREX interaction plane is calculated in the Appendix. The polarisation of the HHG beam relative to the OHREX plane of incidence and reflection is 10.5° out of the plane. Unlike for the RPM interaction, the OHREX crystal reflection is an entirely linear process and it is therefore acceptable to decompose the laser pulse into its constituents, explicitly, the field incident on the crystal is

$$\mathbf{E}_O = \mathbf{E}_{O,s} + \mathbf{E}_{O,p}. \quad (2.36)$$

After interaction with the crystal the field is

$$\mathbf{E}_{\text{detector}} = \alpha_s(h\nu)\mathbf{E}_{\text{O},s} + \alpha_p(h\nu)\mathbf{E}_{\text{O},p}, \quad (2.37)$$

where $\alpha_i(h\nu)$ is the energy dependent ($h\nu$) amplitude sensitivity of the reflection for s- and p-polarised respectively. Since the two polarisations are orthogonal, the intensity is

$$I = \alpha_s^2(h\nu)|\mathbf{E}_{\text{O},s}|^2 + \alpha_p^2(h\nu)|\mathbf{E}_{\text{O},p}|^2. \quad (2.38)$$

Noting that $\alpha_i^2(h\nu)$ are the calibration factors, $G_i(h\nu)$, and that

$$|\mathbf{E}_{\text{O},s}| = |\mathbf{E}_{\text{O}}| \sin \phi \quad (2.39)$$

and

$$|\mathbf{E}_{\text{O},p}| = |\mathbf{E}_{\text{O}}| \cos \phi, \quad (2.40)$$

where ϕ is the angle out of the interaction plane,

$$I_{\text{detector}} = (G_s(h\nu) \sin^2 \phi + G_p(h\nu) \cos^2 \phi) |\mathbf{E}_{\text{O}}|^2 = F(h\nu) |\mathbf{E}_{\text{O}}|^2, \quad (2.41)$$

where $F(h\nu) = (G_s(h\nu) \sin^2 \phi + G_p(h\nu) \cos^2 \phi)$ is the energy dependent calibration factor for this OHREX orientation.

Figure 2.4 is a typical calibrated signal from the quartz (10 $\bar{1}1$) crystal, ready for comparison to the theoretical prediction.

Shots were also taken through the OHREX port, we had hoped to capture the beam divergence however, the beam was larger than initially expected and we were unable to distinguish much. Mention saturation.

Once done all this analysis, present the data.. Integrated signal across crystal, discuss no harmonics but that is expected and then present the final table and discuss.

Include a table detailing error contributions? Also need to add reflectivity error to the rest.

Discuss mirrored targets and brems emission.

Then go back and do the theory. then sims.

Also in sims look at reconstructing a filtered pulse

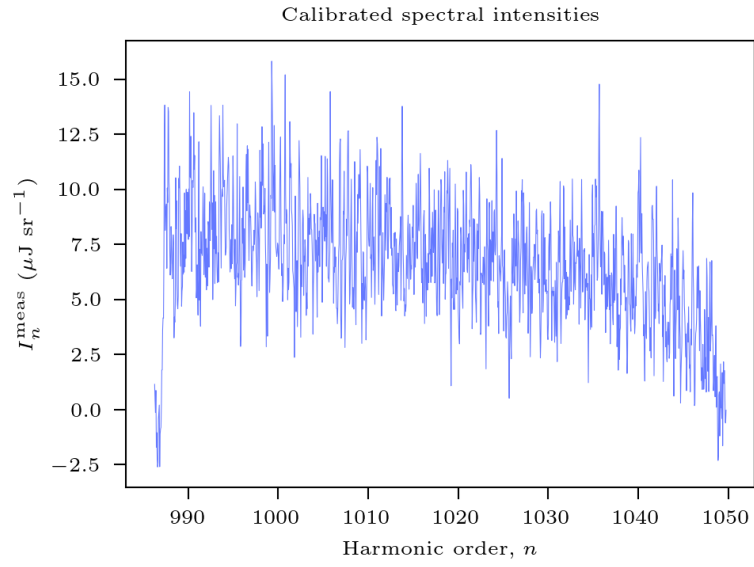


Figure 2.4: Typical (SP1, PMMA) ORION experiment calibrated IP response for the quartz ($10\bar{1}1$) crystal.

Appendices

References

- [1] S C Wilks et al. *Absorption of Ultra-Intense Laser Pulses*. 1992.
- [2] Henri Vincenti. “Achieving Extreme Light Intensities Using Optically Curved Relativistic Plasma Mirrors”. In: *Physical Review Letters* 123.10 (Sept. 3, 2019). PMID: 31573299.
- [3] H. Vincenti et al. “Optical Properties of Relativistic Plasma Mirrors”. In: *Nature Communications* 5 (Mar. 11, 2014), p. 3403. PMID: 24614748.
- [4] A. P.L. Robinson et al. “Relativistically Correct Hole-Boring and Ion Acceleration by Circularly Polarized Laser Pulses”. In: *Plasma Physics and Controlled Fusion* 51.2 (2009).
- [5] A. P.L. Robinson, D. H. Kwon, and K. Lancaster. “Hole-Boring Radiation Pressure Acceleration with Two Ion Species”. In: *Plasma Physics and Controlled Fusion* 51.9 (2009).
- [6] A. L. Meadowcroft, C. D. Bentley, and E. N. Stott. “Evaluation of the Sensitivity and Fading Characteristics of an Image Plate System for X-Ray Diagnostics”. In: *Review of Scientific Instruments* 79.11 (Nov. 11, 2008), p. 113102.
- [7] D. O. Golovin et al. “Calibration of Imaging Plates Sensitivity to High Energy Photons and Ions for Laser-Plasma Interaction Sources”. In: *Journal of Instrumentation* 16.02 (Feb. 2021), T02005.
- [8] N. Izumi et al. “Application of Imaging Plates to X-Ray Imaging and Spectroscopy in Laser Plasma Experiments (Invited)”. In: *Review of Scientific Instruments* 77.10 (Oct. 23, 2006), 10E325.
- [9] Krzysztof W Fornalski. “Simple Empirical Correction Functions to Cross Sections of the Photoelectric Effect, Compton Scattering, Pair and Triplet Production for Carbon Radiation Shields for Intermediate and High Photon Energies”. In: *Journal of Physics Communications* 2.3 (Mar. 22, 2018), p. 035038.
- [10] P. Beiersdorfer et al. “Lineshape Spectroscopy with a Very High Resolution, Very High Signal-to-Noise Crystal Spectrometer”. In: *Review of Scientific Instruments* 87.6 (June 1, 2016).
- [11] M. J. MacDonald et al. “Absolute Throughput Calibration of Multiple Spherical Crystals for the Orion High-Resolution X-ray Spectrometer (OHREX)”. In: *Review of Scientific Instruments* 92.2 (Feb. 1, 2021). PMID: 33648146.
- [12] N. Hell et al. “Calibration of the OHREX High-Resolution Imaging Crystal Spectrometer at the Livermore Electron Beam Ion Traps”. In: *Review of Scientific Instruments* 87.11 (Nov. 1, 2016), p. 11D604.

- [13] B. L. Henke, E. M. Gullikson, and J. C. Davis. “X-Ray Interactions: Photoabsorption, Scattering, Transmission, and Reflection at $E = 50\text{--}30,000$ eV, $Z = 1\text{--}92$ ”. In: *Atomic Data and Nuclear Data Tables* 54.2 (July 1, 1993), pp. 181–342.